


## Article

# Numerical Studies of the Influence of Flue Gas Recirculation into Primary Air on NO<sub>x</sub> Formation, CO Emission, and Low-NO<sub>x</sub> Waterwall Corrosion in the OP 650 Boiler

Bartłomiej Hernik <sup>1,\*</sup> , Piotr Brudziana <sup>2</sup>, Radosław Klon <sup>2</sup> and Marek Pronobis <sup>1</sup>

<sup>1</sup> Department of Power Engineering and Turbomachinery, Silesian University of Technology, Konarskiego 18, 44-100 Gliwice, Poland; marek.pronobis@polsl.pl

<sup>2</sup> RAFAKO Innovation, ul. Łąkowa 33, 47-400 Racibórz, Poland; piotr.brudziana@rafako.com.pl (P.B.); radoslaw.klon@rafako.com.pl (R.K.)

\* Correspondence: bartlomiej.hernik@polsl.pl; Tel.: +48-32-237-1196

**Abstract:** Numerical calculations of the innovative flue gas recirculation (FGR) system through an inactive coal pulverizer for a 40% load of the OP 650 boiler at the Jaworzno III Power Plant were carried out. The research was conducted to determine the effect of FGR on the formation of NO<sub>x</sub>, CO emissions, and low-NO<sub>x</sub> waterwall corrosion. Using numerical modelling, the influence of the place of injection of recirculated flue gas on the formation of NO<sub>x</sub> was also investigated. The tests were carried out based on data from the boiler monitoring system and calculation results using a 0-dimensional model. Modelling of the FGR was performed for five variants. FGR equalized the temperature in the furnace, eliminating temperature peaks in the burner belt. Moreover, FGR did not increase the CO content in the flue gas and reduced the O<sub>2</sub> concentration in the area zone of pulverized coal combustion. For FGR systems, the emission of NO<sub>x</sub> below 200 mg/m<sup>3</sup><sub>n</sub> for 6% O<sub>2</sub> in dry flue gas was kept. This proves that the recirculation helps to meet the BAT (best available techniques) requirements for NO<sub>x</sub> emissions. It has also been shown that FGR does not pose a risk of low-NO<sub>x</sub> corrosion in the next 20 years.

**Keywords:** flue gas recirculation; combustion; numerical simulations; NO<sub>x</sub> emission



**Citation:** Hernik, B.; Brudziana, P.; Klon, R.; Pronobis, M. Numerical Studies of the Influence of Flue Gas Recirculation into Primary Air on NO<sub>x</sub> Formation, CO Emission, and Low-NO<sub>x</sub> Waterwall Corrosion in the OP 650 Boiler. *Energies* **2024**, *17*, 2227. <https://doi.org/10.3390/en17092227>

Academic Editor: Pedro J. Coelho

Received: 27 March 2024

Revised: 25 April 2024

Accepted: 27 April 2024

Published: 6 May 2024



**Copyright:** © 2024 by the authors. Licensee MDPI, Basel, Switzerland. This article is an open access article distributed under the terms and conditions of the Creative Commons Attribution (CC BY) license (<https://creativecommons.org/licenses/by/4.0/>).

## 1. Introduction

One of the possible ways to reduce the emission of NO<sub>x</sub> in boilers, in addition to air staging [1,2], is flue gas recirculation (FGR). It consists of supplying flue gas to the combustion chamber of the boiler. FGR reduces and equalizes the temperature in the furnace, eliminating temperature peaks in the burner region and preventing the secondary formation of NO<sub>x</sub> in the final part of the furnace [3]. In addition, recirculation reduces the O<sub>2</sub> concentration in the combustion zone. The limitation of the use of FGR is the share of O<sub>2</sub> in the flame in the burner zone. If the O<sub>2</sub> concentration is reduced too much, the mixture may stop burning. However, in pulverized coal (PF) boilers, the ratio of excess air in the recirculated flue gas is high. In addition, the coal itself contains 8–12% O<sub>2</sub>, which increases the share of O<sub>2</sub> in the combustion zone. Flue gas recirculation is used as an additional element of modernization in PC boilers to maintain the required superheated steam temperatures at low loads. This excludes the need to increase the ratio of excess air in the combustion chamber, which would interfere with the NO<sub>x</sub> reduction process [4]. The recirculated flue gas increases the flue gas velocity in the area of superheaters, with convection characteristics typical of most solutions. In [5], the influence of the degree of FGR on the content of CO and NO<sub>x</sub> in the flue gas was examined in a laboratory combustion chamber. It has been shown that, with the growth in the rate of FGR and the heat load of the furnace, and the reduction in combustion air number λ, the reduction in NO<sub>x</sub> increases. On the contrary, increasing the recirculation rate and the load increases the amount of CO

in the flue gas. It has been shown in [6] that FGR reduces  $\text{NO}_x$  emissions while increasing CO levels. As a result of recirculation, unfavorable temperature peaks above 1600 °C, which significantly promote thermal  $\text{NO}_x$  production, are reduced to a relatively safe level (1400–1450 °C) to limit the formation of thermal  $\text{NO}_x$ . Another approach to the use of FGR is also possible. In [7], a numerical study of the impact of FGR on the emission of ultrafine ash particles during the combustion of pulverized coal was presented. It has been shown that FGR has a powerful impact on both the particle number density and the size distribution of ultrafine ash particles over PC combustion. For a recirculation rate of 10%, the density number of ultrafine ash grain grows, and the volume mean particle size reduces compared to the case without recirculation. In turn, [8] presents the results of a numerical simulation of a 660 MW coal-fired ultra-supercritical PC boiler. It has been shown that the emission of both  $\text{NO}_x$  and CO decreases with the increase in the recirculation rate. Increasing the recirculation rate can also reduce the unburnt carbon. The influence of the degree of FGR on the combustion instability characteristics and the  $\text{NO}_x$  emission of the gas flame in a 350 kW industrial boiler was presented in [9]. As the recirculation rate rises from 0 to 20%,  $\text{NO}_x$  emissions are reduced by approximately 85%. Combustion instability occurred at high recirculation rates, above 10%. On the other hand, [10] presents the optimization of the aerodynamics and FGR of a 550 MW cyclone-type boiler. The simulation results showed that high-temperature zones in the kiln can be effectively eliminated due to the adapted design of the recirculation system. The impact of FGR conditions on the operation of a boiler with a fluidized bed in the oxy-combustion technology with an air separation unit,  $\text{CO}_2$  compression, and purification unit, and indirect supercritical  $\text{CO}_2$  circulation was studied in [11]. By lowering the temperature of the recirculated flue gas from 90 °C to 40 °C, the concentration of input  $\text{O}_2$  in the combustion chamber increased from 34.7 to 38.5% by volume. The efficiency of the boiler (the ratio of the useful heat output to the total energy input) was 99.6%, and the overall net efficiency of the cycle was 43.1%. It was shown in [12] that the place of introduction of the recirculated flue gas and over-fire air has a significant impact on the temperature profile, combustion efficiency, and  $\text{NO}_x$  emission in a boiler with a circulating fluidized bed (CFB). In turn, in [13], the influence of flue gas recirculation on the efficiency and  $\text{NO}_x$  emission in a waste-burning boiler was examined. Compared to the operation of the boiler without flue gas recirculation, the  $\text{NO}_x$  concentration at the boiler outlet drops from 209.54 mg/m<sup>3</sup> to 126.15 mg/m<sup>3</sup> when the FGR valve is fully opened. A new FGR system was proposed for a 600 MW coal-fired boiler [14]. It has been shown that, for various load conditions, the temperature of the reheated steam increases with an increasing recirculation rate, while coal consumption first decreases, and then increases. The optimization results show that a lower recirculation rate and relatively high coal consumption are urged for high-load conditions, while a higher recirculation rate and relatively lower coal input are suitable for low-load conditions. In [15], the influence of the exhaust gas recirculation rate on the combustion process and  $\text{NO}_x$  formation in a cement rotary kiln with a capacity of 5000 t/d was numerically analyzed. It has been shown that, as the recirculation rate grows, the flame extends and the high-temperature zone reduces. When the recirculation ratio increased from 0% to 27%, the maximum furnace centerline  $\text{NO}_x$  concentration and outlet  $\text{NO}_x$  concentration decreased by 392 ppm and 343 ppm, respectively. In [16], exhaust gas recirculation in the main burner was introduced in a down-fired furnace with a power of 600 MWe. Increasing the recirculation rate has been shown to reduce  $\text{NO}_x$  emissions while worsening fuel burnout. When balancing  $\text{NO}_x$  emissions and burnout, a 12.5% exhaust gas recirculation provides an optimal low- $\text{NO}_x$  combustion with  $\text{NO}_x$  emissions reduced to approximately 600 mg/m<sup>3</sup> (6%  $\text{O}_2$ ) plus high burnout. Taking into account the occurrence of low- $\text{NO}_x$  corrosion, there are several studies on this phenomenon. In [17], it was noticed, for a waterwall tube in conditions where  $\text{O}_2 < 0.5\%$  and  $\text{CO} > 2\%$ , similar to the reducing zone atmosphere, the high-temperature corrosion rate may be much higher than in the case of the presence of  $\text{H}_2\text{S}$  or  $\text{HCl}$  in the flue gas. In [18], numerical studies were carried out to investigate the effect of wall-protecting air on combustion and high-temperature corrosion in a 300 MWe PC utility

boiler with opposed burners. The protection air decreased the peak of the CO and H<sub>2</sub>S content, and also greatly lowered the zone of high CO and H<sub>2</sub>S levels near the side walls. The protection air had little effect on the flue gas temperature and NO<sub>x</sub> concentration at the furnace outlet and showed a marked growth in unburnt carbon. In turn, [19] examined losses in the waterwalls of a pulverized coal-fired boiler and developed appropriate rate correlations for corrosion mechanisms. Rate correlations are based on published study results and investigations executed in a pilot-scale test chamber. The validation results of the numerical model are also presented. In [20], the results of the research on co-operation in the operation of a porous wall with air staging, performed to prevent high-temperature corrosion, were presented. The advantages of a porous wall element should be used. It is also very important to increase the disruption of the coal dust flow and regulate the oxygen concentration in the reduction zone. Preliminary experimental results show that this configuration can simultaneously achieve high-temperature corrosion prevention, high combustion efficiency, and low NO<sub>x</sub> emissions.

The article presents the results of multi-variant numerical studies of a new concept of recirculation of the flue gas into the primary air flowing through the mill. The research was carried out in order to determine the effect of such FGR on the formation of NO<sub>x</sub>, CO emissions, and waterwall corrosion in the OP 650 boiler (PC boiler, with natural circulation in the evaporator, with a capacity of 650 t/h of superheated steam). The tests were carried out for 40% of the unit's power (91.6 MWe) based on the results of calculations using a 0-dimensional model.

## 2. Description of Modelling and Numerical Methods

To reduce NO<sub>x</sub> emissions, the low-emission burners type NR3 manufactured by FORTUM were installed in the boiler, supplemented with OFA (over-fire air) nozzles. The OP 650 boiler is a drum, two-pass boiler with natural water circulation in the evaporator, coal-fired, with reheating. The dimensions of the furnace are 16.78 m × 8.91 m. The boiler is fired by 24 front-swirl burners and equipped with four mills. The connection diagram of mills with burners is shown in Figure 1.

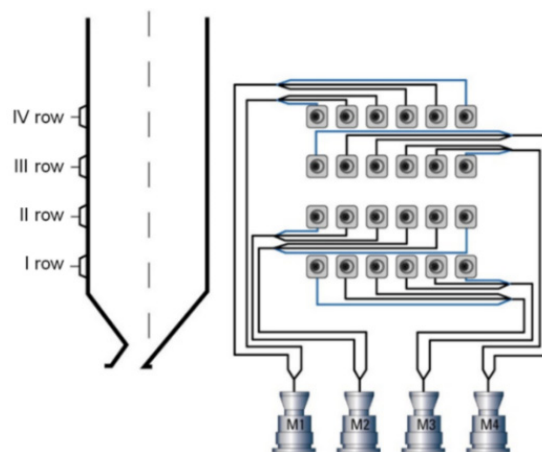


**Figure 1.** Arrangement of burners with mills.

Above the burner belt, on the front and rear walls, there are two levels of OFA nozzles. The nozzles on the first level are equipped with air-swirling vanes. The concept of the new FGR system was developed at RAFAKO Racibórz from Poland [21] and shown in Figure 2. In the existing FGR systems, the flue gas is pumped through additional flue gas fans. In the proposed solution, the additional fans were not necessary and the existing primary air fans for coal mills were used for this purpose. Thus, recirculating flue gas will be introduced to the boiler through the inactive pulverizers to coal burners. This takes place at a unit load below 140 MW and the boiler's operation on two mill units. By supplying flue gas together with primary air to active mill units, it is also possible to reduce the O<sub>2</sub> content

in the dust-air mixture. The solution is very cheap in terms of investment. An additional advantage of such a solution is that it is easier to maintain low  $\text{NO}_x$  emissions with a reduced specific power. In coal-fired boilers, such a procedure can be very helpful in the case of insufficiently high steam temperatures. The recirculation of the flue gas partially to the combustion furnace increases the flue gas stream flowing over the superheater tubes, which intensifies the heat exchange in the surfaces with convection characteristics. Therefore, the main purpose of using the FGR system is to ensure the required steam temperatures, especially the reheat steam, when operating with significantly reduced boiler power. The influence of the injection site of the recirculated flue gas on the formation of  $\text{NO}_x$  was also numerically modelled. It is important to maintain the BAT conclusions. The BAT document [22] is a reference point for the values of emission standards. When burning coal in the boiler with a nominal thermal power above 300 MW, the permissible  $\text{NO}_x$  emission value is  $200 \text{ mg/m}^3_n$ , with an  $\text{O}_2$  concentration in the exhaust gases of 6%. Numerical studies were carried out using the Ansys Fluent code [23]. The research of combustion was performed to determine the effect of FGR to primary air on the formation of  $\text{NO}_x$ .

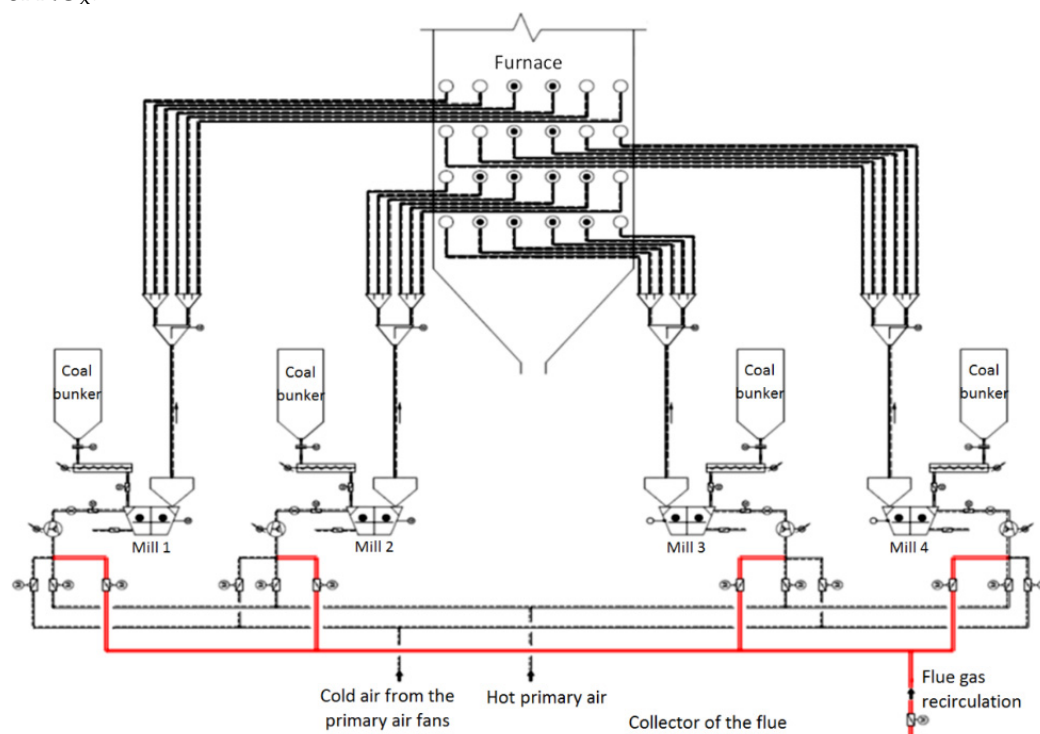


**Figure 2.** The idea of the FGR system in the OP 650 boiler in Jaworzno III Power Plant.

The tests were carried out for 40% of the unit's capacity (91.6 MWe). Flue gas recirculation was performed for five cases:

1. The third and fourth row of coal burners are in operation; recirculation to the second row—case rec1
2. The third and fourth row of coal burners are in operation; recirculation to the first row—case rec2
3. The second and third row of coal burners are in operation; recirculation to the fourth row—case rec3
4. The second and third row of coal burners are in operation; recirculation to the first row—case rec4
5. The third and fourth row of coal burners are operating with 18%  $\text{O}_2$  in the primary air by mixing with part of the recirculation flue gas; recirculation to the second row—case rec1A.

The geometry and numerical mesh of the low-emission NR3 burner are shown in Figure 3.



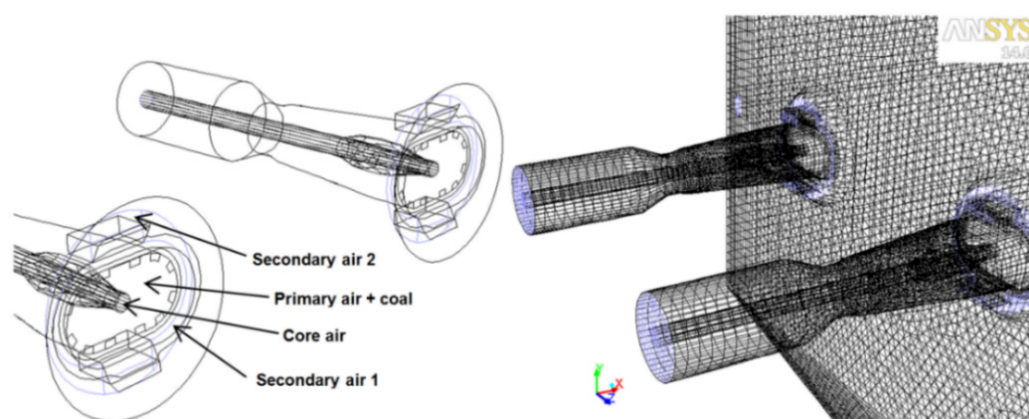


**Figure 3.** Geometric model and numerical mesh of the NR3 burner.

A geometric model of the OP 650 boiler RAFAKO Racibórz from Poland, including individual stages of the live-steam (LS) and reheated-steam (RS) superheaters, is shown in Figure 4. The model also includes a protection air system (PAS) protecting the rear and side walls of the boiler against low- $\text{NO}_x$  corrosion and urea injection for the non-catalytic reduction of  $\text{NO}_x$ .

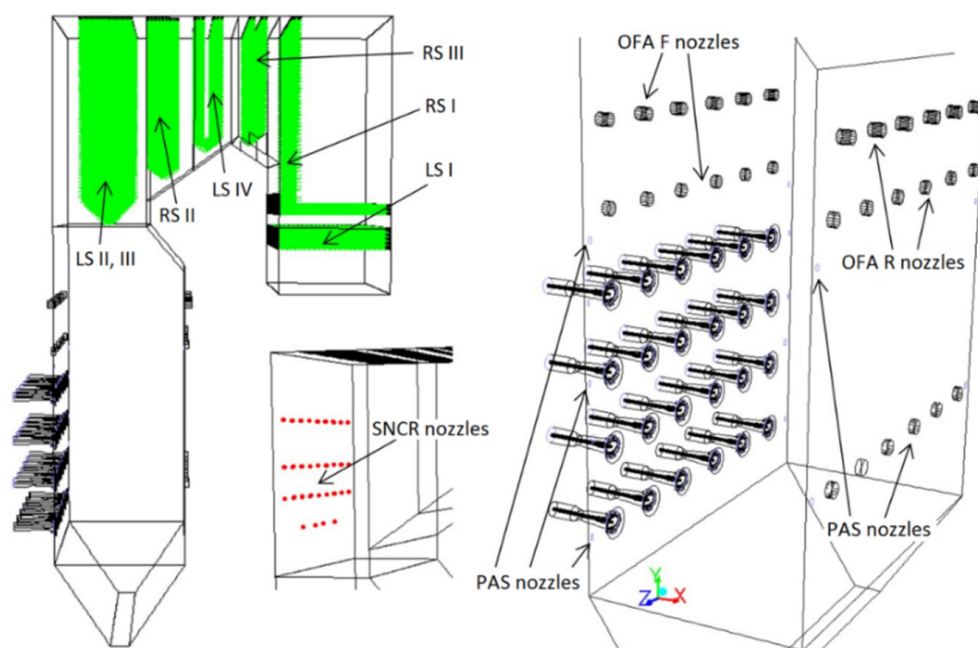


**Figure 4.** Geometric model of the OP 650 boiler.

The numerical mesh, consisting of 6,576,794 numerical cells, is shown in Figure 5. The superheaters were managed as a porous area constructed in the form of sheets, heated with flue gas as described in [24].

The coal analysis is shown in Table 1, while the coal granulation is presented in Table 2. The polydispersity number describes the level of homogeneity of the pulverized coal particle size. The unburnt carbon loss (furnace loss) is more significant if the boiler is operated with coal with a low polydispersity number.

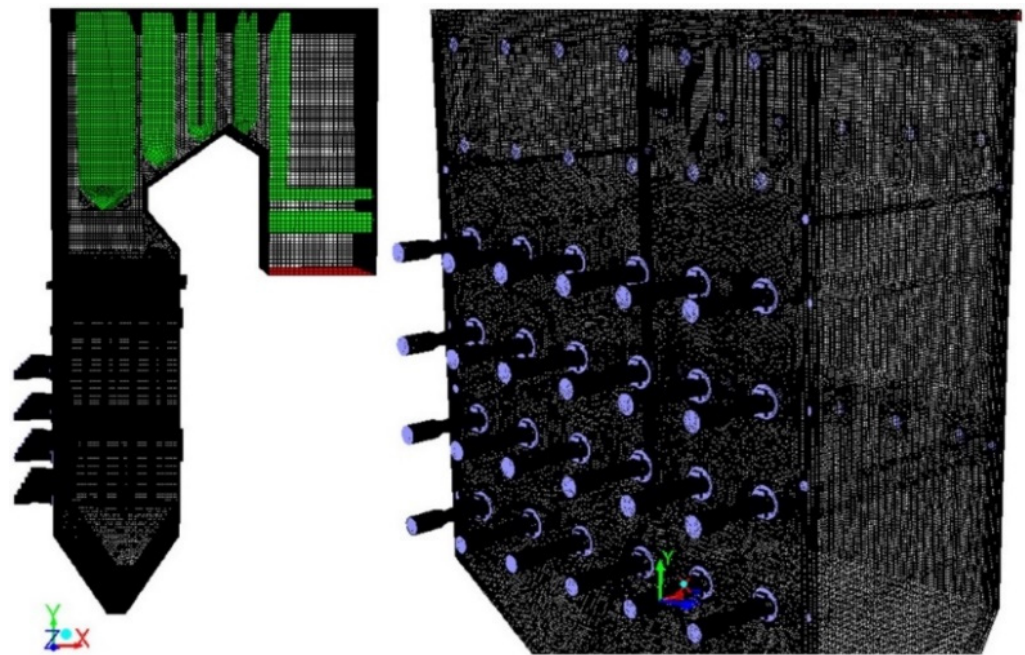


**Figure 5.** Numerical mesh of the boiler.

**Table 1.** Fuel analysis.

Data	Unit	Coal M	Coal H
Net calorific value	kJ/kg	20,504	22,005
Ash	wt%	14.5	12
Moisture	wt%	15	12
Volatile matter	wt%	43.1	48.5
Ultimate analysis		As received	
Carbon, C	wt%	54.93	58.84
Hydrogen, H	wt%	3.3	3.6
Oxygen, O	wt%	10.33	11.83
Sulfur, S	wt%	1.1	1.0
Nitrogen, N	wt%	0.84	0.68

**Table 2.** Coal granulation.

Data	Unit	Value
Sieve residue (cumulative percentage retained) on sieve 90 $\mu\text{m}$	%	23.15
Sieve residue 200 $\mu\text{m}$	%	3.1
The average diameter of the pulverized coal	$\mu\text{m}$	61
Uniformity (polydispersity) number	-	1.05

Table 3 shows the assumptions used in the numerical code for the considered cases. Cases 60% M and 60% H mean a 60% loaded boiler fired with coal M and H, with upper mills (M1, M2, and M4) running. The FGR calculations were carried out for coal H. There is 20% of the flue gas flow recirculated.

**Table 3.** The air and the fuel flows for considered cases.

Data	Unit	60% M	60% H	Rec 1, Rec 2	Rec 3, Rec 4
Coal flow	kg/s	17.28	16.05	10.56	10.26
Primary air flow	kg/s	62.34	62.34	48.78	48.78
Recirculated flue gas flow	kg/s	-	-	23.34	22.69

Table 3. Cont.

Data	Unit	60% M	60% H	Rec 1, Rec 2	Rec 3, Rec 4
Secondary air flow 1	kg/s	34.91	34.45	20.64	19.1
Secondary air flow 2	kg/s	17.52	17.29	10.36	9.6
Core air flow	kg/s	8.24	8.24	2.99	2.99
OFA F air flow	kg/s	2.51	2.51	1.62	1.62
OFA R air flow	kg/s	7.18	7.18	4.31	4.31
PAS air flow	kg/s	7.39	7.32	4.19	3.95
Primary air temperature	°C	109	109	109	109
Secondary air temperature	°C	262	262	251	245

To modelling turbulent flow, solving the Navier–Stokes (N–S) equations is crucial. The Reynolds-averaged Navier–Stokes (RANS) technique, which involves formulating behavioral equations for the time means of temperature, pressure, and velocity, is often used for these calculations. However, because each averaging of nonlinear N–S equations creates more unknowns, it is necessary to introduce a model that will close the system of equations and enable their solution. Therefore, the numerical simulations use the k-epsilon realizable model for turbulence. This model submits two variables—turbulence kinetic energy ( $k$ ) and dissipation of energy ( $\epsilon$ ). Therefore, it is possible to account for the turbulent viscosity ( $\mu_t$ ) responsible for the growth in viscosity at turbulent flows. The model gives the best results (within the k-epsilon “family”) in both simple and complex flows [25,26]. The transportation statement for  $k$  and  $\epsilon$  are as follows:

$$\frac{\partial}{\partial t}(\rho k) + \frac{\partial}{\partial x_j}(\rho k u_j) = \frac{\partial}{\partial x_j} \left[ \left( \mu + \frac{\mu_t}{\sigma_k} \right) \frac{\partial}{\partial x_j} \right] + G_k + G_b - \rho \epsilon - Y_M + S_k, \quad (1)$$

$$\frac{\partial}{\partial t}(\rho \epsilon) + \frac{\partial}{\partial x_j}(\rho \epsilon u_j) = \frac{\partial}{\partial x_j} \left[ \left( \mu + \frac{\mu_t}{\sigma_k} \right) \frac{\partial \epsilon}{\partial x_j} \right] + \rho C_1 S \epsilon - \rho C_2 \frac{\epsilon^2}{k + \sqrt{\nu \epsilon}} + C_{1\epsilon} \frac{\epsilon}{k} C_{3\epsilon} G_b - S_\epsilon \quad (2)$$

where  $G_k$  describes the production of turbulence kinetic energy as a result of the velocity gradient,  $G_b$  is the production of turbulence kinetic energy due to buoyancy,  $Y_M$  describes the contribution of dilation oscillations in compressible turbulence to the general dissipation rate, and  $C_2$  and  $C_{1\epsilon}$  are constants, while  $\sigma_k$  and  $\sigma_\epsilon$  are the corresponding Prandtl numbers for  $k$  and  $\epsilon$ .

Turbulence and chemical reactions have a significant interplay in pulverized coal boilers. To accurately model this process, solving the fluid flow equations and including extra  $N$  equations associated with the reaction products is necessary. These equations can be noted as standard transportation equations:

$$\frac{\partial \rho Y_k}{\partial t} + \frac{\partial \rho u_i Y_k}{\partial x_i} = \frac{\partial}{\partial x_i} \left( \rho D_k \frac{\partial Y_k}{\partial x_i} \right) + \dot{\omega}_k \text{ for } k = 1, 2 \dots N, \quad (3)$$

where  $D_k$  is the coefficient of diffusion,  $Y_k$  is the mass fraction of the individual reaction components, and  $\dot{\omega}_k$  is the chemical reaction rate and is the sum of the production of each ingredient in the  $M$  chemical reactions of the process.

To fully describe the combustion process mathematically, an energy equation is essential. It is possible to express it by the transport equation for temperature:

$$\frac{\partial \rho T}{\partial t} + \frac{\partial \rho u_i T}{\partial x_i} = \frac{\partial}{\partial x_i} \left( \frac{\lambda}{C_p} \cdot \frac{\partial T}{\partial x_i} \right) + \dot{\omega}_T, \quad (4)$$

$$\dot{\omega}_T = \sum_{k=1}^N \Delta h_k \dot{\omega}_k, \quad (5)$$

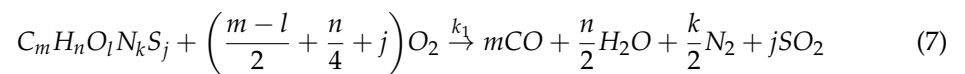
where  $\Delta h_k$  is the formation enthalpy of component  $k$ ,  $\lambda$  is the thermal diffusion coefficient, and  $C_p$  is the heat capacity.

The flue gas density is determined by adding up the densities of the individual components. As for the dynamic viscosity, it is calculated based on empirical formulae that take temperature into account [26]. As a combustion model, a Finite Rate/Eddy Dissipation (FR/ED) model was applied [27]. The reaction rate is determined by using both the Eddy Dissipation Model (EDM) equations and the Arrhenius equation for the kinetic constants of global reactions. This model permits slower reactions to be retained in cases where the mixing process is intensive, although the reaction should not take place. The smaller value of the following equation is selected for the calculation:

$$\dot{\omega}_{kj} = \min\left(\dot{\omega}_{kj}, \dot{\omega}_{kj}^{Arr}\right), \quad (6)$$

where  $\dot{\omega}_{kj}$  are the equations of the EDM model, and  $\dot{\omega}_{kj}^{Arr}$  is the Arrhenius equation.

The EDM equations are the key to controlling the combustion process by regulating the degree of mixing. This is determined based on the kinetic energy of turbulence  $k$  and its degree of dissipation  $\varepsilon$  [25]. The EDM equations are indeed based on the concept of vortex decay time, which is essentially the  $k/\varepsilon$  mixing time. Below are the reactions of volatile fraction combustion and CO oxidation. It is worth noting that coefficients  $m$ ,  $n$ ,  $l$ ,  $k$ , and  $j$  were obtained based on coal composition.



Discrete Ordinates (DOs) were used as the radiation model to solve the radiation heat transport equations. The isotropic phase dissipation function was applied, and the model includes radiation heat transfer between flue gas and coal particles, as well as between boiler walls and coal particle surfaces. The absorption coefficient was calculated using the weighted sum of grey gases model (WSGGM). The discrete phase model (DPM) was used to simulate the coal particle flow, predicting particle trajectories with the Lagrange approach using the average fluid velocity in turbulent flow:

$$\frac{du_p}{dt} = F_d(u - u_p) + \frac{g_x(\rho_p - \rho)}{\rho_p} + F_x \quad (9)$$

The first term represents the frictional force, the second represents the gravitational force, and the third represents any additional forces that may be present.

$$F_d = \frac{18\mu}{\rho_p d_p^2} \frac{C_D Re}{24} \quad (10)$$

$$Re = \frac{\rho d_p (u_p - u)}{\mu}, \quad (11)$$

where  $u$  is the fluid velocity,  $u_p$  is the velocity of the particle,  $\mu$  is the dynamic viscosity of the fluid,  $\rho$  is the density of the fluid,  $\rho_p$  is the density of the particle,  $d_p$  is the diameter of the particle,  $Re$  is relative Reynolds number, and  $C_D$  is drag coefficient.

The sphericity of the coal grains was taken and the drag coefficient is determined by the equation:

$$C_D = a_1 + \frac{a_2}{Re} + \frac{a_3}{Re^2}, \quad (12)$$

where  $a_1$ ,  $a_2$ , and  $a_3$  are constants specified by Morsi and Aleksander in [28].

A two-way relation between the fuel grains and fluid was considered. Additionally, the Rosin–Rammler–Sperling distribution [4] was applied to model the coal particles. The

Single Rate model was utilized to compute the coal devolatilization, assuming that the degassing rate depends on the amount of volatile substances in the fuel particle [29].

$$-\frac{dm_p}{dt} = k[m_p - (1 - f_{v,0})(1 - f_{w,0})m_{p,0}], \quad (13)$$

$$k = Ae^{-\left(\frac{E}{RT}\right)}, \quad (14)$$

where  $m_p$  is the molecule mass,  $f_{v,0}$  is the initial mass fraction of the volatiles included in the particle,  $f_{w,0}$  is the mass fraction of the evaporating substance in the particle,  $m_p$  is the initial molecule mass,  $k$  is the kinetic velocity,  $A$  is the pre-exponential factor, and  $E$  is the energy activation.

The coal combustion rate is determined by the kinetic–diffusion model, where the rate of the surface reaction is presumed to be determined by the kinetics or rate of diffusion. The equation used to calculate the coal combustion rate is [30,31]:

$$\frac{dm_p}{dt} = -A_p p_{ox} \frac{D_0 R}{D_0 + R}, \quad (15)$$

where  $D_0$  is the diffusion rate coefficient,  $m_p$  is the molecule mass,  $A_p$  is the particle surface area,  $p_{ox}$  is the partial pressure of the oxidant compounds in the gas surrounding the particle, and  $R$  is the reaction rate, including the effect of the chemical reaction on the inner surface of the coal particle and diffusion leaks.

The oxidation reaction of char to  $\text{CO}_2$  can be represented by the following equation:



When coal is burned, three oxygen–nitrogen compounds are made:  $\text{N}_2\text{O}$ ,  $\text{NO}$ , and  $\text{NO}_2$ . The most significant number of  $\text{NO}$  is produced, followed by  $\text{NO}_2$ , and the smallest amount of  $\text{N}_2\text{O}$ . The formation rate of  $\text{NO}_x$  is temperature-dependent. To account for temperature and composition changes, the probability density fraction (PDF) was utilized. A fuel and thermal  $\text{NO}_x$  approach was used. The Zeldovich scheme [32] was employed to estimate the generation of thermal  $\text{NO}_x$ :



A third reaction has been proposed for the formation of thermal  $\text{NO}_x$  under conditions comparable to stoichiometric and fuel-rich compounds [33–35]:



Most of the thermal  $\text{NO}_x$  is generated after the combustion process. Therefore, accepting the thermic stability and balance of stable constituents, O atoms, and OH free radicals, the thermal  $\text{NO}_x$  formation mechanism can be isolated from the primal process of combustion [32]. The concentrations of O [36] and OH [37] were determined using a partial equilibrium approach. The calculations assumed that the nitrogen in the coal was split into volatiles and char. The nitrogen in the char is converted to  $\text{NO}$  [38], while the volatile nitrogen produces  $\text{HCN}$  and  $\text{NH}_3$ . According to the Winters study [39], using a 9:1 split ratio of  $\text{HCN}/\text{NH}_3$  for coal provides more accurate  $\text{NO}_x$  predictions than considering only one indirect product.

The calculations use the reduced kinetic approach presented by Brouwer et al. [40] in the SNCR model:







The study by Rota et al. [41] investigated the two-step mechanism of urea decomposition:



The numeric model was confirmed by employing a zero-dimensional model (0D). The results obtained from the 0D model were used as a reference for the numerical research of flue gas recirculation. The 0D model is established on the thermal and flow balance computations of the whole boiler, including its three dimensions (depth, width, and height). All heat exchangers are also taken into account along with dimensions such as tube diameter and length, tube bank pitch, number of tubes, and rows of tube. The model considers the heat transfer between flue gas and the operating fluid. The temperature of the flue gas and the operating fluid beyond each heat exchange surface is calculated in the 0D model. It also delivers knowledge about the velocity of the flue gas and the operating fluid. These calculations were carried out using a homemade program, based on the procedures presented in [42–44]. According to the [45] standard, as well as from the monitoring data of the distributed control system, and from other measurements, the input data were taken. The temperature at the furnace exit was calculated using a methodology presented in [42,46], while the convection pass of the boiler was determined by utilizing a methodology based on research conducted at the Silesian University of Technology, as presented in [45]. A comprehensive analysis of the computational model's accuracy is presented in [45], and many modernizations of boilers have been developed, applying the depicted method, confirming its believability. The 0D model based on measurements is adequate for examining the operating parameters of boilers built after modernization [47].

### 3. Calculation Results with Discussion

#### 3.1. Numerical Model Verification

Since the boiler did not operate at 40% load, the base reference case for numerical model verification was the case of a 60% boiler load. Two coals marked as M and H were used to validate the model to obtain a greater reliability of the numerical model. For the reference case of a 60% boiler load, information from the distributed boiler control system about the CO and NO<sub>x</sub> content in the flue gas at the model exit and unburnt coal in the fly ash and slag were obtained. Using the 0D model, the temperatures behind each heat exchanger in the flue gas path and at the outlet from the combustion chamber and the model exit were also verified. The O<sub>2</sub> content at the combustion chamber outlet and the model's exit, as well as the CO and NO<sub>x</sub> content at the combustion chamber outlet, were also verified employing the 0D model. The results of the verification for a 60% load, fired with M and H coal with the 0D model, are presented in Table 4. The flue gas temperature in the characteristic planes of the boiler is shown in Figure 6, while the collation of the area-weighted average flue gas temperatures in cross-sections as a relationship of the flue gas path is shown in Figure 7.

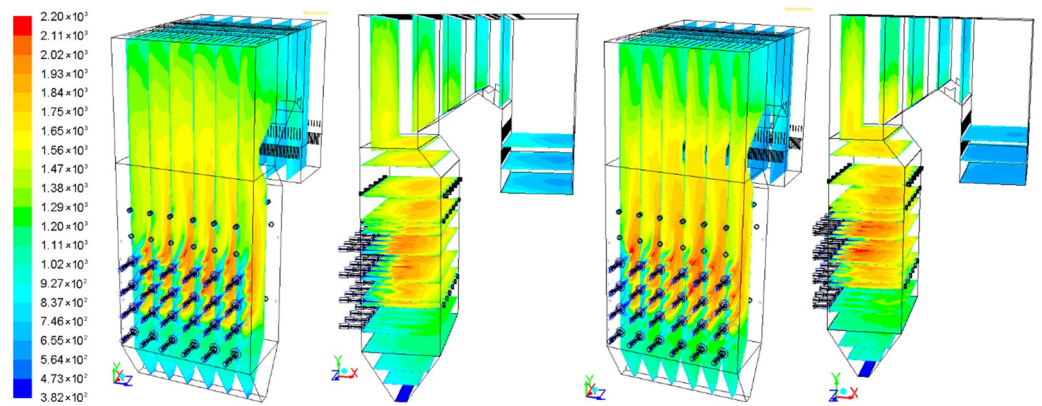


Figure 6. Flue gas temperature [K] in selected planes for M (left) and H (right) coals.

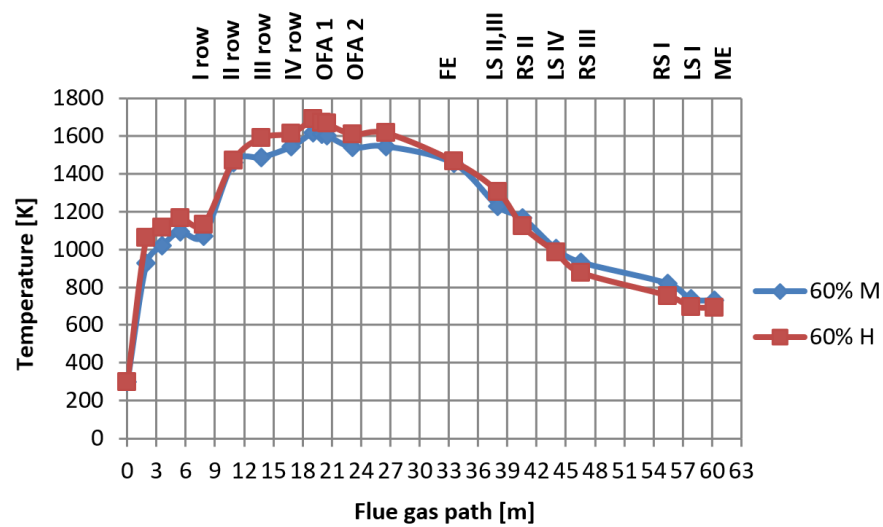
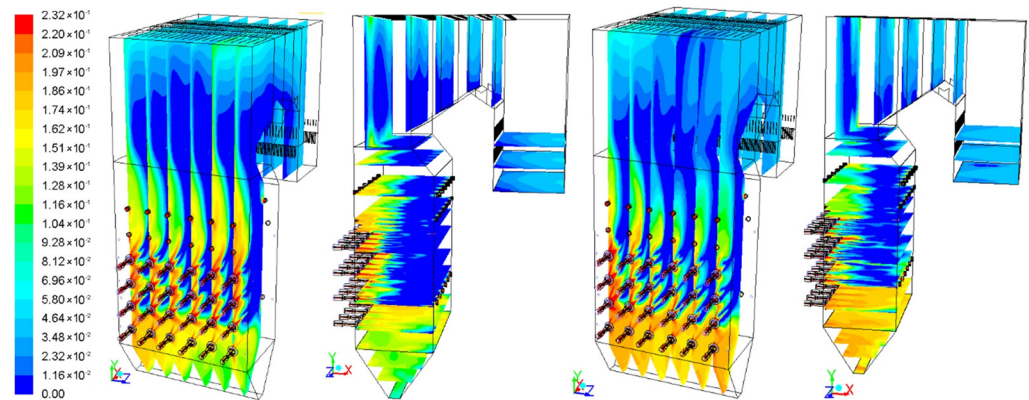


Figure 7. The area-weighted average flue gas temperature [K] in cross-sections as a function of flue gas path for 60% M and 60% H cases.

Changing the fuel slightly affects the flue gas temperature in the area of the burners. In this area, the flue gas temperature reaches higher values for the case of the 60% H—coal with a higher calorific value. For both cases, the flue gas temperature receives the highest value above the fourth row of burners, in front of the OFA nozzles. The flue gas temperature beyond the level of the OFA nozzles slightly increases, because the air supplied by the OFA nozzles burns the unburnt coal particles remaining as a consequence of sub-stoichiometric combustion (fuel-rich condition—insufficient oxygen). As heat is transferred between the flue gas and the heat exchangers, the temperature of the flue gas decreases along their path. Behind the combustion chamber in the flue gas path, the flue gas temperature for the case of 60% M usually reaches higher values than for the case of 60% H.

The O<sub>2</sub> mass fraction in the flue gas in the typical planes of the boiler is shown in Figure 8. A lack of O<sub>2</sub> can be observed in the vicinity of the rear wall OFA nozzles. This is due to the course of the combustion in this area, resulting from the so-called flame licking of the rear wall (see Figure 6). Therefore, a high O<sub>2</sub> content can be observed in the flue gas at the level of the front wall OFA nozzles. The core air from the first level of burners supports the combustion of the fuel and lowers the underburning in the slag hopper—Table 4.



**Figure 8.** The  $O_2$  mass fraction in selected planes for M (left) and H (right) coals.

The collation of the area-weighted average  $O_2$  contents in the flue gas in cross-sections as a function of the flue gas path is shown in Figure 9.

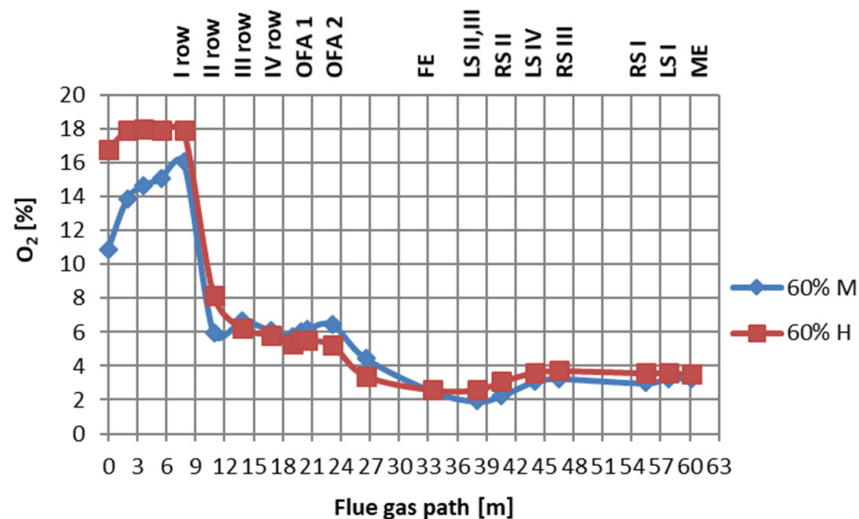


**Figure 9.** The area-weighted average  $O_2$  content [%] in cross-sections as a function of flue gas path for 60% M and 60% H cases.

The average  $O_2$  content in the flue gas decreases from the second row of burners. An increased share of  $O_2$  can be observed in the planes of the OFA nozzles. Behind the OFA nozzles, the average  $O_2$  content in the flue gas decreases, which is related to the afterburning of unburnt fuel particles in this area in accordance with Reaction (16). This is also due to the participation of  $O_2$  in the CO oxidation reaction according to the course of Reaction (8). The change of fuel slightly affects the differences in the average  $O_2$  content in the flue gas in the area of the burners. In the combustion area, the average  $O_2$  contents in the flue gas reaches lower values for the case of 60% H. On the other hand, at the model outlet, the average  $O_2$  content in the flue gas is 60% M lower for the case. The increase in the  $O_2$  content at the final section of the flue gas path results from boiler leaks, i.e., from sucking in false air.

Figure 10 shows the CO contents in the dry flue gas in the typical planes of the boiler. The appearance of CO in the vicinity of the burners is the result of the degassing of coal particles and the combustion of volatile matter. The presence of CO is even an effect of the combustion of pulverized coal grains in the absence of  $O_2$  in the combustion region. The highest CO value was obtained in the planes of the third and fourth row of burners.

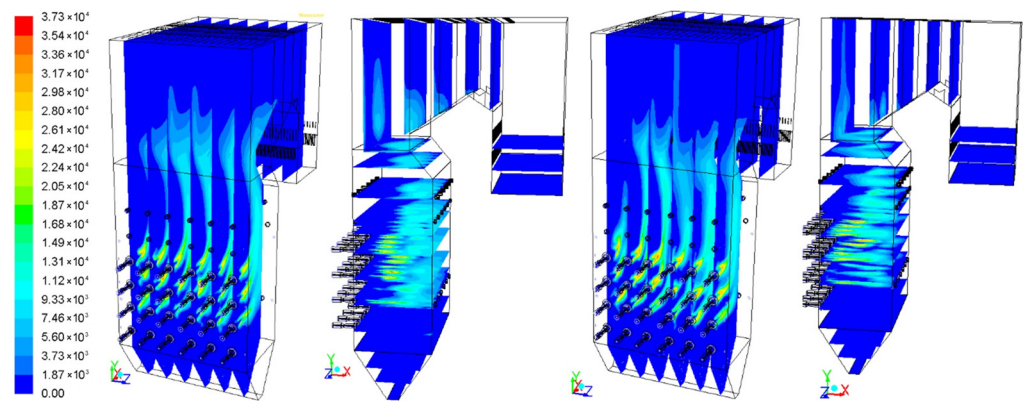


Figure 10. The CO contents [mg/m<sup>3</sup> 6% O<sub>2</sub>] in selected planes for M (left) and H (right) coals.

The collation of the area-weighted average content of CO in the flue gas in cross-sections as a function of the flue gas path is shown in Figure 11.

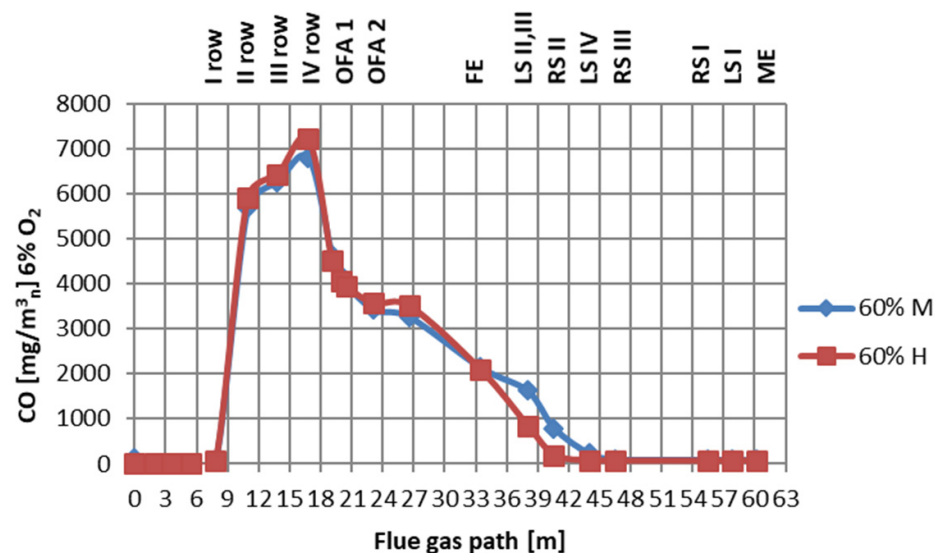


Figure 11. The area-weighted average CO content [mg/m<sup>3</sup> 6% O<sub>2</sub>] in cross-sections as a function of the flue gas path for 60% M and 60% H cases.

The decrease in the CO content behind the fourth row of burners is related to the afterburning of unburnt sub-stoichiometric fuel particles in the area of the burners. This is also due to the course of the oxidation Reaction (8). In the area of the burners, slight differences in the mean CO contents in the flue gas due to the change of fuel can be observed. In the combustion area, the mean content of CO in the flue gas reaches lower values for the case of 60% M. On the other hand, at the model outlet, the average CO contents in the flue gas is lower for the 60% H case.

Figure 12 shows the NO<sub>x</sub> contents in the typical planes of the boiler. A lower NO<sub>x</sub> concentration is observed for variant M, where there is a lower temperature in the combustion region than in variant H—Figure 6. The lower contents of O<sub>2</sub> in the flue gas in the sub-stoichiometric combustion zone for variant M in relation to case H (Figures 8 and 9) also results in the formation of a smaller amount of NO<sub>x</sub> in case M.

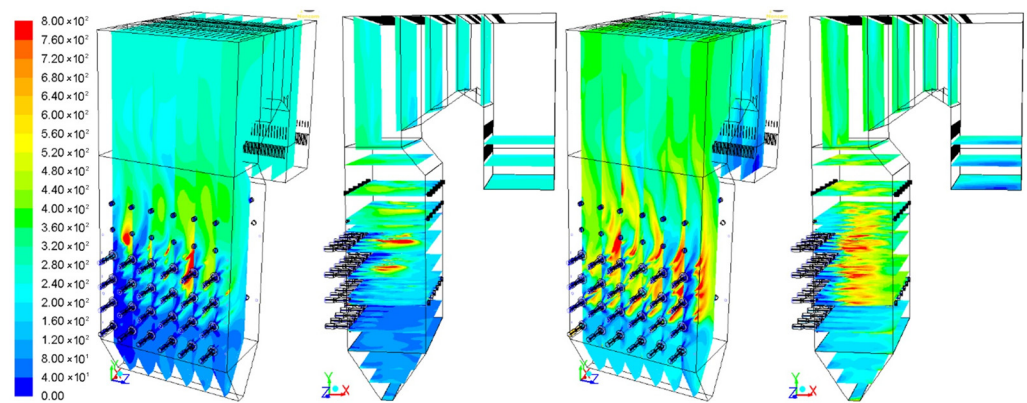


Figure 12. The NO<sub>x</sub> content [mg/m<sup>3</sup><sub>n</sub> 6% O<sub>2</sub>] in selected planes for M (left) and H (right) coals.

The collation of the area-weighted average contents of NO<sub>x</sub> in the flue gas in cross-sections as a function of the flue gas path is shown in Figure 13.

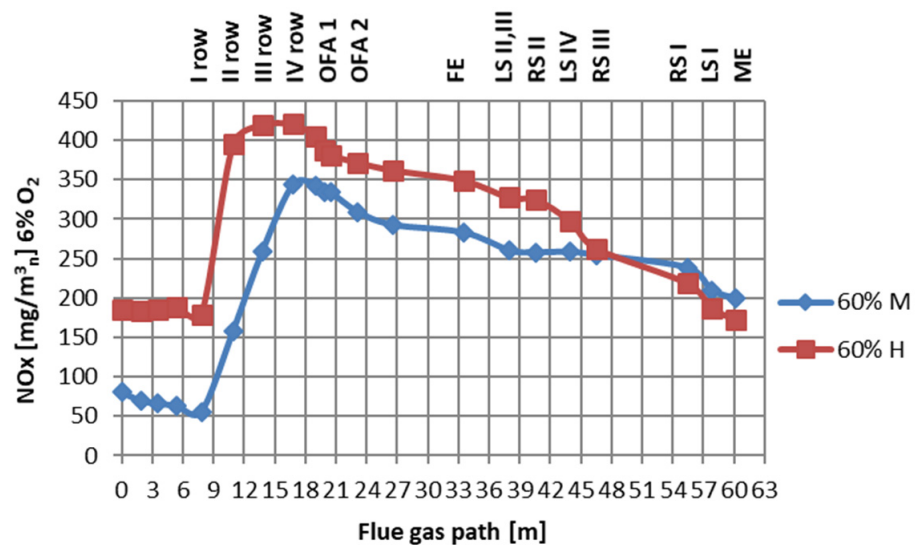


Figure 13. The area-weighted average NO<sub>x</sub> content [mg/m<sup>3</sup><sub>n</sub> 6% O<sub>2</sub>] in cross-sections as a function of the flue gas path for 60% M and 60% H cases.

The change of fuel affects the differences in the average contents of NO<sub>x</sub> in the flue gas in the boiler along the flue gas path. The average NO<sub>x</sub> content in the flue gas reaches higher values for the case of 60% H, but only up to the area of the third reheater stage. This is due to the higher flue gas temperature for this case in this area—the thermal mechanism of nitrogen oxide formation prevails. On the other hand, in the area behind the third reheater stage in the flue gas path, the average NO<sub>x</sub> content in the flue gas is higher for the case of 60% M. M coal has a higher nitrogen content in the fuel, which, despite temperatures that are not too high, contributes to the increased NO<sub>x</sub> content in this area—the fuel mechanism of nitrogen oxide formation prevails.

### 3.2. Numerical Research for Flue Gas Recirculation

The flue gas temperature in the characteristic planes of the boiler is shown in Figure 14. The collation of the area-weighted average flue gas temperatures in the cross-sections as a relationship of the flue gas path for recirculation cases is shown in Figure 15.



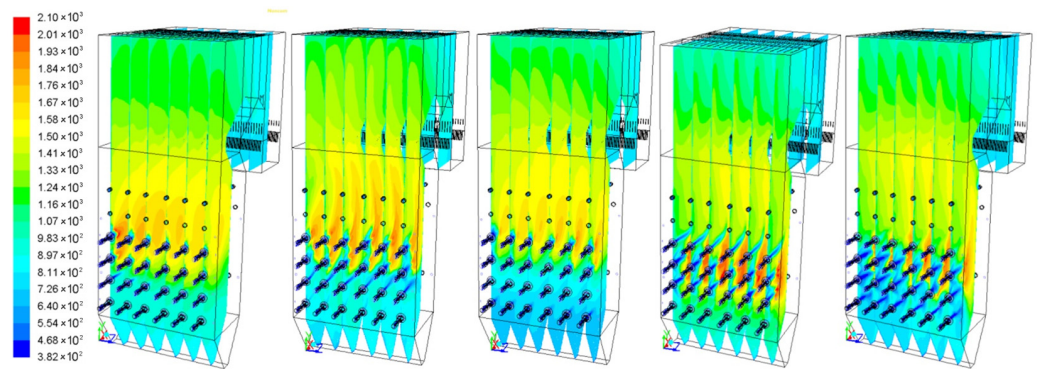


Figure 14. Flue gas temperature [K] in selected planes—from left: rec1, rec1A, rec2, rec3, and rec4.

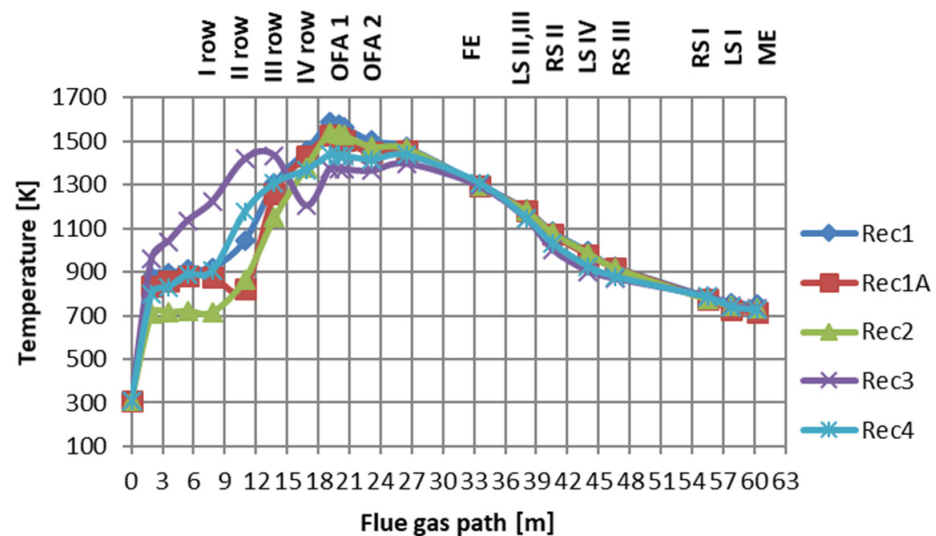


Figure 15. The area-weighted average flue gas temperature [K] in cross-sections as a function of flue gas path for rec1, rec1A, rec2, rec3, and rec4.

Due to the reduced  $O_2$  in the primary air, for the case of rec1A, the combustion is more extended along the height of the combustion chamber compared to the case of rec1. In the case of rec1, the flame core (high-temperature region) is lowered compared to the case of rec2. Similarly, case rec3 shows the lowest-position flame core compared to case rec4. Reducing the flue gas temperature for case rec3 in the plane of the fourth row of burners results from the recirculation of flue gas to this row. The high flue gas temperature in the area up to the third row of burners is the result of the boiler operating on the middle burners (second and third row of burners). The lowest flue gas temperatures in the bottom section of the burner belt can be observed for case rec2. Relatively low flue gas temperatures in this area are also observed for case rec1A. The most increased flue gas temperatures above the fourth row of burners occurred for cases rec1, rec1A, and rec2, where the two upper rows of burners (III and IV) operate on coal. With the heat exchange between flue gas and heat exchangers, the flue gas temperature drops about the same for all cases through the flue gas path.

The  $O_2$  mass fraction in the flue gas in the characteristic planes of the boiler is shown in Figure 16. The collation of the area-weighted average contents of  $O_2$  in the flue gas cross-sections as a function of the flue gas path for recirculation cases rec1, rec1A, rec2, rec3, and rec4 is shown in Figure 17.

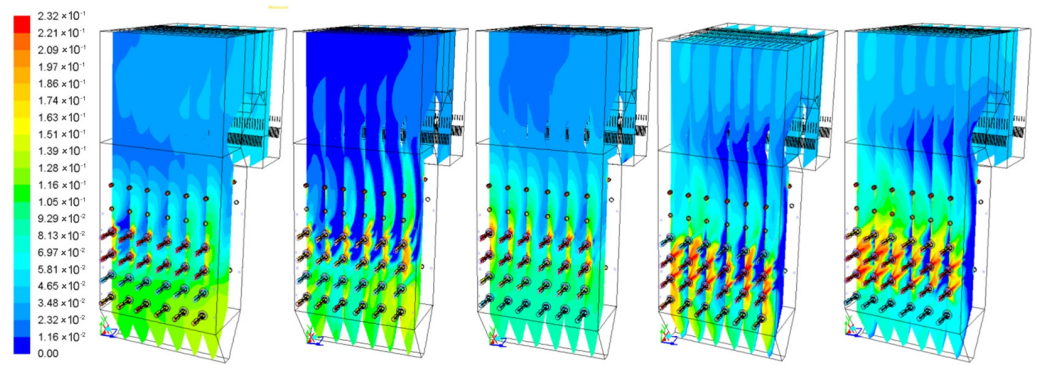


Figure 16. Mass fraction of O<sub>2</sub> in selected planes—from left: rec1, rec1A, rec2, rec3, and rec4.

In case rec2, the contents of O<sub>2</sub> in the flue gas decreased in the plane of the first row of burners compared to case rec1. For case rec3, the O<sub>2</sub> content above the fourth row of burners is reduced compared to case rec4. For case rec4, in the plane of the first row of burners, a decrease in the O<sub>2</sub> content is observed compared to case rec3. The O<sub>2</sub> proportion in the flue gas is also influenced by which rows of burners are fed with coal during flue gas recirculation. For cases rec4 and rec2, the flue gas is recirculated to the first row of burners, but, in case rec4, a lower share of O<sub>2</sub> in the flue gas in the first row of burners is observed. The lowest average contents of O<sub>2</sub> in the flue gas in the lower part of the burner belt occurred for case rec4. A relatively low average concentration of O<sub>2</sub> in the flue gas in this area is also observed for case rec3. The highest average O<sub>2</sub> content in the flue gas in the lower part of the burner belt appeared for cases rec1 and rec1A.

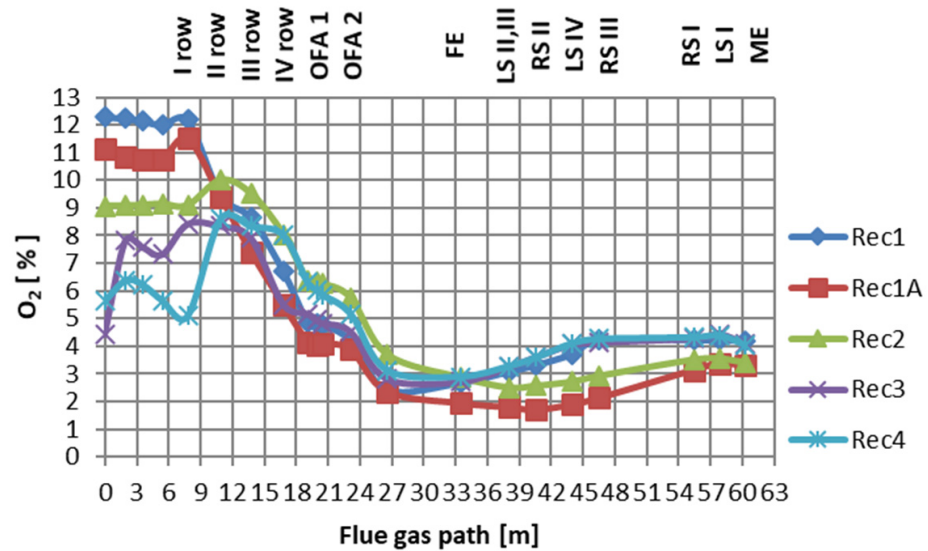
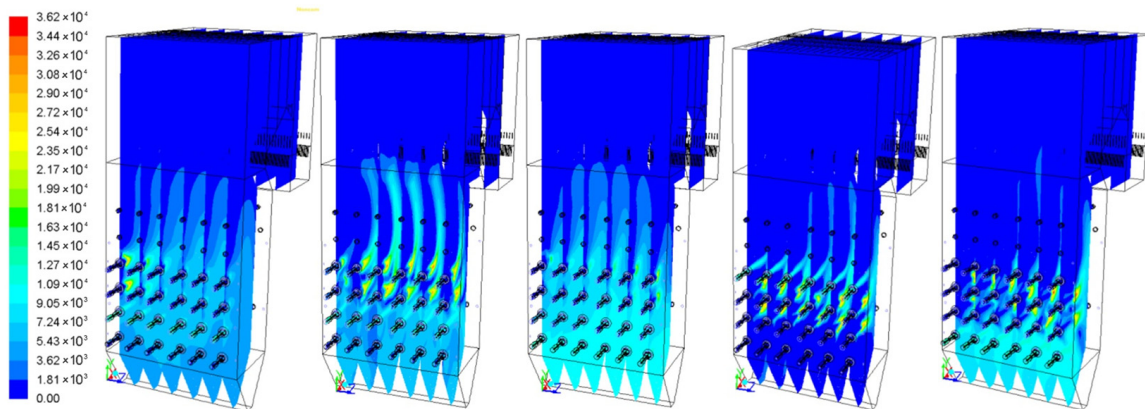


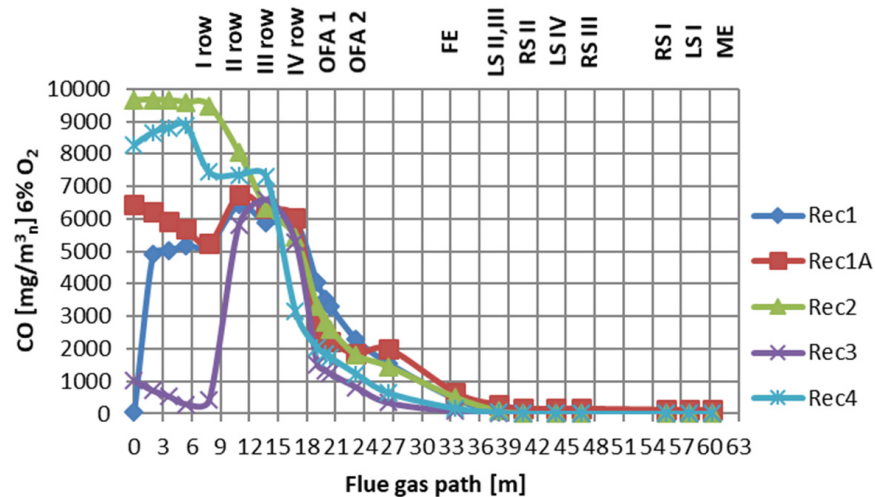
Figure 17. The area-weighted average O<sub>2</sub> content [%] in cross-sections as a function of flue gas path for rec1, rec1A, rec2, rec3, rec4.

The increase in the O<sub>2</sub> in the region between the furnace outlet and the model outlet results from boiler leaks, i.e., from sucking in false air. Figure 18 shows the CO contents in the flue gas in the typical planes of the boiler. A comparison of the area-weighted average share of CO in cross-sections in the flue gas path for recirculation cases rec1, rec1A, rec2, rec3, and rec4 is presented in Figure 19.



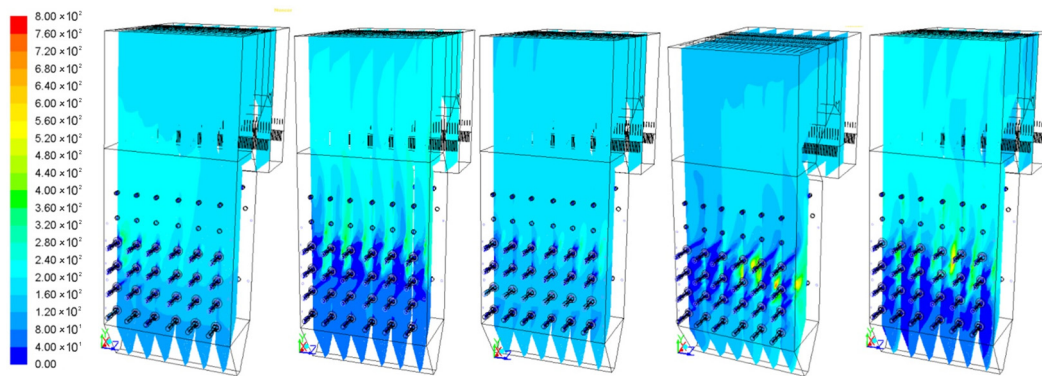
**Figure 18.** The CO content [ $\text{mg}/\text{m}^3_{\text{n}} 6\% \text{O}_2$ ] in selected planes—from left: rec1, rec1A, rec2, rec3, and rec4.

In case rec2, the concentration of CO in the flue gas in the first row of burners increases compared to case rec1. In the case of rec1A, with less  $\text{O}_2$  in the primary air, less CO was produced in the surface of the second row of burners according to the volatile matter combustion Reaction (7). In turn, the reduced  $\text{O}_2$  content in this case, in accordance with Reaction (8), causes an increase in the share of CO at the combustion chamber exit and from the model exit—see Table 4. The reduced  $\text{O}_2$  content in the case of rec1A also increases the fly ash and slag in relation to case rec1—see Table 4. For case rec3, the CO content above the fourth row of burners increases compared to case rec4. For case rec4, in the surface of the first row of burners, the CO content increased in relation to case rec3. The level of active coal burners during the FGR operation also affects the proportion of CO in the flue gas. For case rec4, the contents of CO decreased in the plane of the first row of burners compared to case rec2. In the lower part of the burner belt, the highest average CO content was achieved for case rec2 and the lowest average CO content was recorded for case rec3.



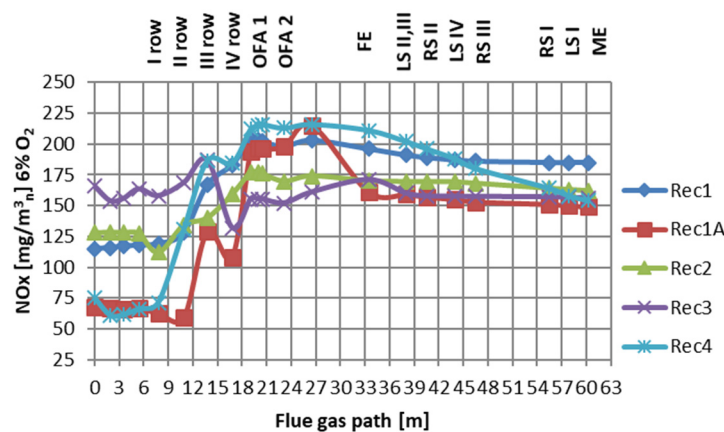
**Figure 19.** The area-weighted average CO content [ $\text{mg}/\text{m}^3_{\text{n}} 6\% \text{O}_2$ ] in cross-sections as a function of flue gas path for rec1, rec1A, rec2, rec3, and rec4.

Figure 20 shows the  $\text{NO}_x$  contents in the dry flue gas in the typical planes of the boiler.



**Figure 20.** The NO<sub>x</sub> content [mg/m<sup>3</sup><sub>n</sub> 6% O<sub>2</sub>] in selected planes—from left: rec1, rec1A, rec2, rec3, and rec4.

In case rec2, a higher content of NO<sub>x</sub> in the flue gas in the first row of burners was noted compared to case rec1. For case rec1A, with less O<sub>2</sub> in the primary air, less NO<sub>x</sub> is produced in the surface of the second row of burners. The reduced O<sub>2</sub> content in this case results in a lowering in NO<sub>x</sub> at the furnace outlet and the outlet from the model—see Table 4. In case rec3, a decrease in the NO<sub>x</sub> content above the fourth row of burners is observed compared to case rec4. For case rec4, a decrease in NO<sub>x</sub> was achieved in the surface of the first row of burners compared to case rec3. The amount of NO<sub>x</sub> is also influenced by which rows of burners are fed with coal during flue gas recirculation. For case rec4, in the surface of the first row of burners, a smaller amount of NO<sub>x</sub> was recorded compared to case rec2. The collection of the area-weighted average contents of NO<sub>x</sub> in the cross-sections of the flue gas as a relationship of the flue gas path for recirculation cases rec1, rec1A, rec2, rec3, and rec4 is presented in Figure 21. In case rec3, the area of the first three rows of burners produces the highest amount of NO<sub>x</sub> compared to the other cases. In the surface of the fourth row of burners, NO<sub>x</sub> reduction occurred in this case. For case rec3, the smallest amounts of NO<sub>x</sub> are produced in the area of OFA nozzles. The highest NO<sub>x</sub> values in the upper part of the burner belt and in the area of OFA nozzles were obtained for case rec4. In all cases, in the plane downstream of the second and third live-steam superheaters (LS II and III), a decrease in NO<sub>x</sub> was recorded as a result of the operation of the SNCR installation.



**Figure 21.** The area-weighted average contents of NO<sub>x</sub> [mg/m<sup>3</sup><sub>n</sub> 6% O<sub>2</sub>] in cross-sections as a function of flue gas path for rec1, rec1A, rec2, rec3, and rec4.

The presented numerical study reasonably reliably reflects the flue gas temperature distribution compared to the zero-dimensional model (0D) and the values obtained from the measurements. The measurement results are derived from the monitoring data of the distributed control system and are presented in Table 4 as (m). The summarized results in



the combustion chamber exit planes and from the model exit planes are shown in Table 4. Numerical effects were received at a level near the computed values. The notation 0D/m means a value obtained using a zero-dimensional model or from measurements. The values obtained from the measurement are marked with (m) in the data column.

**Table 4.** A summary of the outcomes in the combustion chamber exit planes and the model exit plane.

Data	Unit	60% M		60% H		Rec1		Rec1a	Rec2		Rec3		Rec4	
		0D/m	CFD	0D/m	CFD	0D/m	CFD	CFD	0D/m	CFD	0D/m	CFD	0D/m	CFD
O <sub>2</sub> furnace exit	%	2.52	2.5	2.53	2.58	2.75	2.67	1.93	2.75	2.86	2.75	2.71	2.75	2.89
CO 6% O <sub>2</sub> furnace exit	mg/m <sup>3</sup> <sub>n</sub>	2137	-	2086	-	452	650	-	504	-	70	-	163	
NO <sub>x</sub> 6% O <sub>2</sub> furnace exit	mg/m <sup>3</sup> <sub>n</sub>	282	-	349	-	196	161	-	170	-	171	-	211	
O <sub>2</sub> model outlet	%	3.23	3.26	3.25	3.5	3.83	4.2	3.3	3.83	3.4	3.83	4.1	3.83	4.05
CO 6% O <sub>2</sub> model exit (m)	mg/m <sup>3</sup> <sub>n</sub>	97	88.5	97	62	-	46	111	-	5	-	4	-	3
NO <sub>x</sub> 6% O <sub>2</sub> model exit (m)	mg/m <sup>3</sup> <sub>n</sub>	179	199	179	172	-	185	149	-	162	-	156	-	154
Temperature furnace exit	°C	1190	1182	1197	1194	1060	1031	1023	1060	1024	1005	1021	1005	1037
Temperature after LS II, III	°C	985	955	990	1034	890	913	911	890	907	851	871	851	875
Temperature after RS II	°C	839	893	842	850	761	811	800	761	805	726	728	726	758
Temperature after LS IV	°C	743	730	747	711	700	721	706	700	714	659	630	659	653
Temperature after RS III	°C	644	659	647	605	613	651	648	613	646	588	597	588	606
Temperature after RS I	°C	497	547	500	483	474	513	504	474	501	459	515	459	511
Temperature model exit	°C	450	458	452	420	433	475	445	433	462	422	461	422	454
Unburnt carbon in fly ash (m)	%	6.2	3.21	6.2	3.16	-	0.3	1.9	-	0.5	-	0.8	-	0.9
Unburnt carbon in slag (m)	%	3.3	0.95	3.3	1.26	-	0.5	1.1	-	0.8	-	9.4	-	11.2

Similar to [8,48–50], FGR reduces the NO<sub>x</sub> contents in the flue gas at the exit of the combustion chamber and at the outlet of the model. This is noticeable by comparing the cases rec1, rec1A, rec2, rec3, and rec4 with the cases of 60% M and 60% H presented in Table 4. All considered cases obtained NO<sub>x</sub> emissions under 200 mg/m<sup>3</sup><sub>n</sub>, @ O<sub>2</sub> 6%, following the requirements of the BAT document. FGR also reduced the flue gas temperature at the combustion chamber outlet. A comparable tendency of the temperature of the flue gas to decrease is observed in [48,50]. The CO content declines with the growth of the O<sub>2</sub> content. For the recirculation cases, no increase in the contents of CO in the flue gas is observed in relation to the case of 60% H in the zone of pulverized coal combustion. A higher CO concentration is noticeable only for the row of burners through which the recirculated flue gas is fed. In case rec1A, with the O<sub>2</sub> in the primary air reduced to 18%, there is no increase in the contents of CO in the flue gas in the third and fourth row of burners in relation to case of 60% H. That proved the stable combustion in the combustion chamber. The reduced flame temperature caused by FGR may lead to combustion instability [9]. Despite the decrease in O<sub>2</sub> concentration in the region of the third and fourth row of burners, no rapid decrease in the flue gas temperature was observed. Thus, the combustion process proceeds stably without breaking the flame. On the other hand, the unburnt carbon in the fly ash and in the slag increases in relation to case rec1, which is the base for the discussed case rec1A. Therefore, supplying the stream of recirculated flue gas to the furnace through burners that are not fueled with coal does not affect the combustion stability.

### 3.3. Numerical Research of Protection Air Systems

In PC boilers, where primary methods of reducing NO<sub>x</sub> emissions were used, the corrosion of the waterwalls often occurred, causing injury to the tubes and the need for their expensive replacements [4,51,52]. It seems that, even if the contents of O<sub>2</sub> in the flue gas is higher than the CO content, there is no need to worry about rapid corrosion. It is universally assumed that, if the content of O<sub>2</sub> decreases below 1% near the walls of the combustion chamber, then the intensification of corrosion processes should be taken into account. An additional criterion is the presence of CO in the flue gas boundary layer [4]. In Polish boilers, corrosion was observed already at concentrations CO ≈ 0.8%. In order to reduce the intensity of corrosion in the OP 650 boiler, a protective air system (PAS) was used.



The air streams are entered alongside the walls of the burner belt, creating an oxygen-rich boundary layer separating the evaporator tubes from the aggressive components of the flue gas, and protecting against the local occurrence of a reducing atmosphere [18,53].

The content of  $O_2$  and CO in the flue gas boundary layer for the walls of the evaporator was presented in Figure 22 for the 60% case.

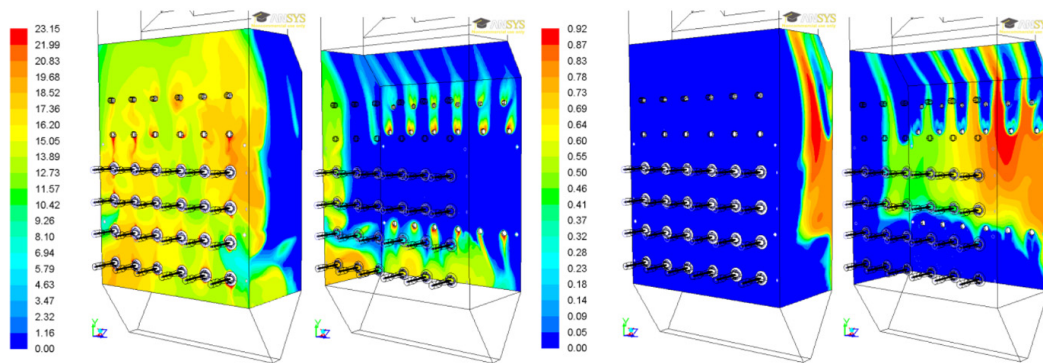


**Figure 22.** The  $O_2$  (left) and CO (right) content [%] for front and left, and rear and right walls—60% M.

For the case of 60% M, the greater part of the right wall is exposed to low- $NO_x$  corrosion. There is no  $O_2$  in the boundary layer of the flue gas. There is a reducing atmosphere, with a CO content of 0.9%. The left wall, on the other hand, is not at risk of corrosion because, despite the lack of  $O_2$ , the CO content in it does not exceed 0.5%. The part of the back wall of the evaporator is at risk. There is no  $O_2$  in the zone between the PAS and the OFA nozzles, but, on the right side, there is CO in an amount of 0.83 to 0.92%.

Figure 23 shows the content of  $O_2$  and CO in the flue gas boundary layer for the walls of the evaporator for the case of 60% H.

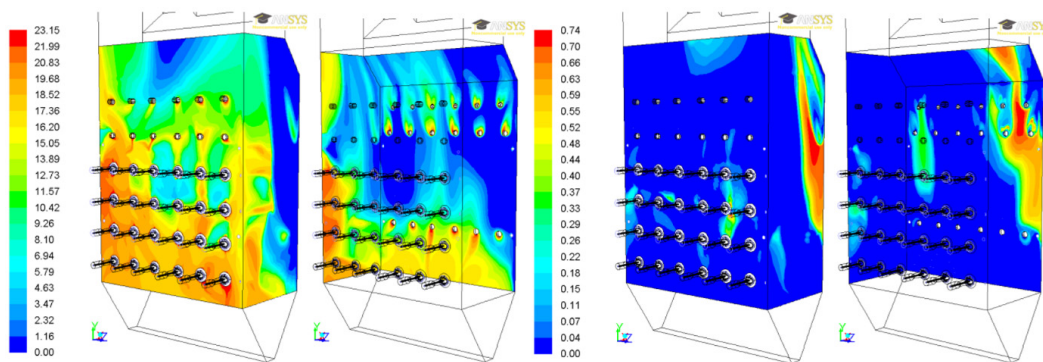


**Figure 23.** The  $O_2$  (left) and CO (right) content [%] for front and left, and rear and right walls—60% H.

For the case of 60% H, the rear part of the right wall is exposed to low- $NO_x$  corrosion. There is a reducing atmosphere with a CO content of 0.74%. The left wall is not exposed to corrosion, because there is a boundary layer containing  $O_2$  and the CO content does not exceed 0.3%. The front wall is also not at risk of corrosion because there is a high concentration of  $O_2$ , despite the CO content of 0.74%. The right part of the back wall of the evaporator is at risk of corrosion. On the right side of the rear wall, in the area between the PAS and OFA nozzles, there is no  $O_2$ , but there is CO in the amount of 0.74%.

Figure 24 shows the percentages of  $O_2$  and CO in the flue gas boundary layer for the walls of the evaporator for the case of rec1. For case rec1, none of the walls is drastically exposed to low- $NO_x$  corrosion. For the rear wall with a CO content of 0.92%, there is a high concentration of  $O_2$  in the flue gas equal to 8%.

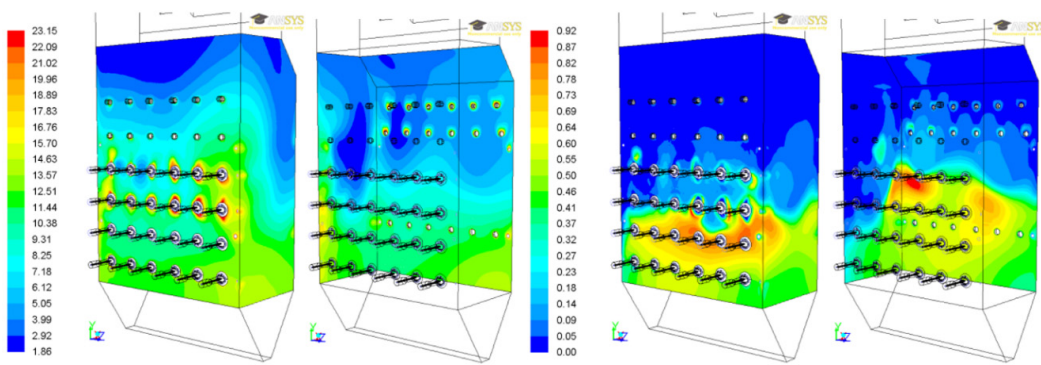


Figure 24. The O<sub>2</sub> (left) and CO (right) content [%] for front and left, and rear and right walls—rec1.

Figure 25 shows the percentages of O<sub>2</sub> and CO in the flue gas boundary layer for the walls of the evaporator for the case of rec1A. For case rec1A, the left and rear walls are not drastically exposed to corrosion. In the areas with a CO content of 1.04%, there is a high concentration of O<sub>2</sub>, equal to about 15%. However, the left wall is at risk of corrosion. In the area of CO occurrence at the level of 1.04%, O<sub>2</sub> is not contained in the boundary layer of flue gas.

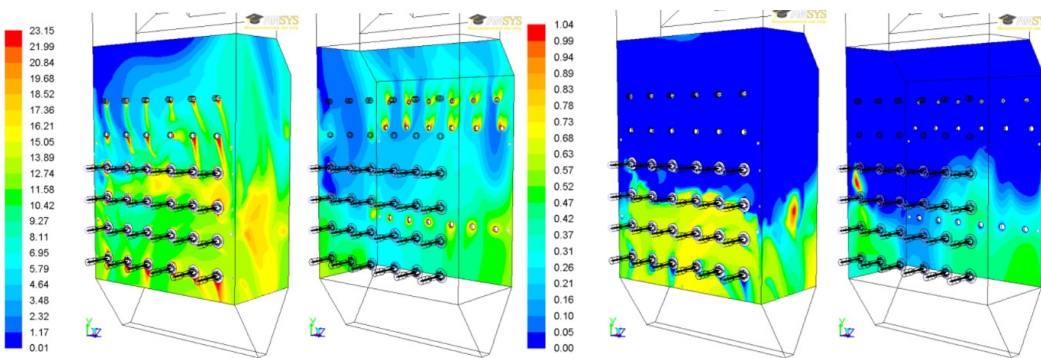


Figure 25. The O<sub>2</sub> (left) and CO (right) content [%] for front and left, and rear and right walls—rec1A.

Figure 26 shows the percentages of O<sub>2</sub> and CO in the flue gas boundary layer for the walls of the evaporator for the case of rec2. For case rec2, none of the walls is drastically exposed to corrosion. In areas with an increased CO content in the amount of 1.11%, there is a high concentration of O<sub>2</sub> equal to 11%.

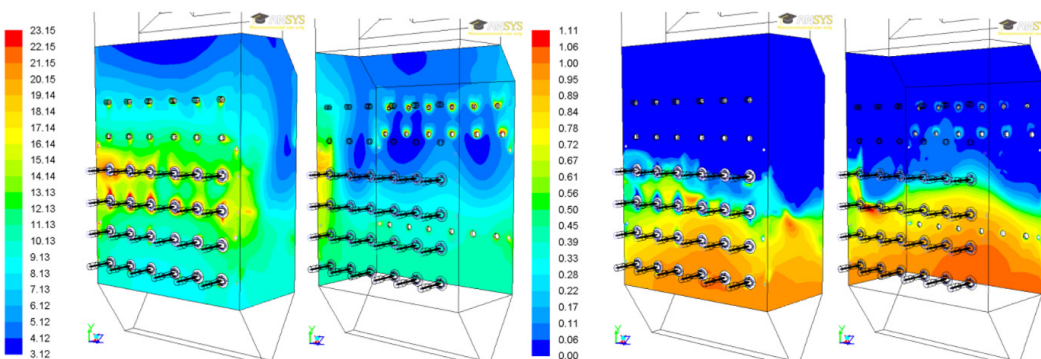


Figure 26. The O<sub>2</sub> (left) and CO (right) content [%] for front and left, and rear and right walls—rec2.

Figure 27 shows the percentage content of O<sub>2</sub> and CO in the flue gas boundary layer for the walls of the evaporator for the case of rec3. For case rec3, a slight rear part of the right wall is exposed to corrosion. In this area, there is no O<sub>2</sub>, but there is a CO content of

0.75%. The left wall is not exposed to corrosion; despite the lack of O<sub>2</sub> in its boundary layer, the concentration of CO does not exceed 0.6%. The rear wall is not drastically exposed to corrosion. Despite the lack of O<sub>2</sub> in the area between the PAS and OFA nozzles, the CO content does not exceed 0.5%.

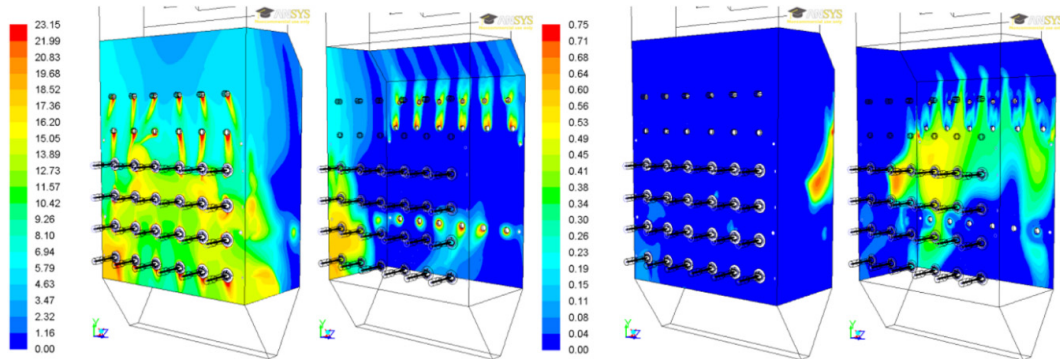


Figure 27. The O<sub>2</sub> (left) and CO (right) content [%] for front and left, and rear and right walls—rec3.

Figure 28 shows the percentage content of O<sub>2</sub> and CO in the flue gas boundary layer for the walls of the evaporator for the case of rec4. For case rec4, a significant part of the right wall is not drastically exposed to low-NO<sub>x</sub> corrosion. In the oxygen-depleted area, the CO content in the boundary layer of the flue gas is a maximum of 0.8%. However, in the area where the CO content is 1%, there is also O<sub>2</sub> in the amount of about 8%. Similarly, the left wall is also not drastically exposed to corrosion. In the oxygen-free area, the CO content is a maximum of 0.75%. The rear wall is at risk of corrosion. In areas without O<sub>2</sub>, the CO content is a maximum of 0.95%.

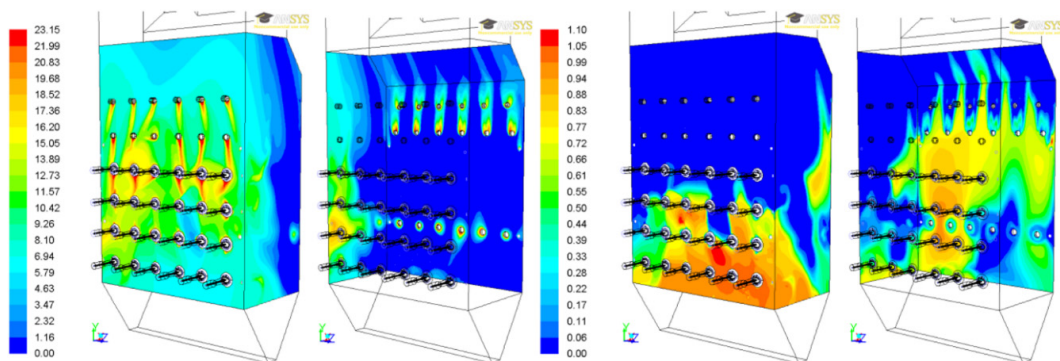


Figure 28. The O<sub>2</sub> (left) and CO (right) content [%] for front and left, and rear and right walls—rec4.

Table 5 below presents the results of the calculations of the corrosion rate of the evaporator tubes according to the methodology contained in [54]:

$$w_{corrCO}^{max} = 17.91[CO] + 7.63 \text{ [nm/h]} \tag{29}$$

Table 5. The tube thickness loss rates due to the low-NO<sub>x</sub> corrosion.

Data	Unit	60% M	60% H	Rec1	Rec1A	Rec2	Rec3	Rec4
$w_{corrCO}^{max}$	nm/h	24.1	20.9	-	26.3	-	21.1	27.3
$w_{corrCO}^{max}$	mm/year	0.211	0.183	-	0.230	-	0.185	0.239
$t_f$	h	207,407	239,425	-	190,430	-	237,389	182,943
CO	%	0.92	0.74	0.92	1.04	1.11	0.75	1.1
O <sub>2</sub>	%	0	0	8	0.01	11	0	0

Table 5 shows the maximum values of carbon monoxide in the flue gas boundary layer for a particular case as CO. The O<sub>2</sub> values refer to the areas where the above-mentioned



maximum CO values occur for a particular case. The evaporator has tubes with a wall thickness of 5 mm. The time  $t_f$  was calculated, after which the tube wall thickness is punctured and a failure occurs, resulting in the shutdown of the power unit. It should be emphasized that FGR does not cause an increased risk of the low-NO<sub>x</sub> corrosion of screens. The values in Table 5 prove that they are not dangerous for a boiler with a maximum remaining operating time of 50,000–70,000 h.

#### 4. Conclusions

The paper shows the results of the numerical research of the combustion process, including flue gas recirculation for a boiler operating in a 200 MW power plant unit. In the control planes of the OP 650 boiler and at the outlet from the model, there is a satisfactory agreement of temperature, O<sub>2</sub>, CO, NO<sub>x</sub>, and unburnt carbon with the values received from the zero-dimensional model and the measurements. It has been shown numerically that FGR reduces and equalizes the temperature in the furnace, eliminating temperature peaks in the burner belt. In addition, it has been shown that FGR reduces the O<sub>2</sub> concentration in the combustion area and also reduces the flue gas temperature at the combustion chamber outlet. Based on the results of numerical calculations, it was shown that FGR reduces the content of CO and NO<sub>x</sub> in the flue gas at the furnace outlet and the model exit. For FGR systems, the emission of NO<sub>x</sub> was kept below 200 mg/m<sup>3</sup><sub>n</sub> @ 6% O<sub>2</sub> in the dry flue gas. This proves that, at a low power of the boiler, FGR will help meet the BAT requirements for NO<sub>x</sub> emissions. Assuming the NO<sub>x</sub> emission criterion, case rec4 is the most advantageous variant of FGR. The analysed FGR, which consists of feeding the exhaust gas to the furnace through inactive mills, will not impair the combustion stability. For the tested cases of boiler operation, there is no risk of low-NO<sub>x</sub> corrosion occurring during the expected life of the boiler. A future research step will be the combustion of a mixture of coal with an alternative fuel or a switch to another fuel.

**Author Contributions:** Conceptualization, P.B.; methodology, B.H. and M.P.; software, B.H.; validation, B.H.; formal analysis, B.H.; investigation, B.H.; resources, B.H.; data curation, P.B. and R.K.; writing—original draft preparation, B.H.; writing—review and editing, B.H. and M.P.; visualization, B.H.; supervision, R.K. and M.P.; project administration, B.H., R.K. and M.P.; funding acquisition, R.K. All authors have read and agreed to the published version of the manuscript.

**Funding:** This research was funded by the Polish National Centre for Research and Development, project “Low-emission innovative technologies of the upgrade of coal-fired power stations with 200 MW power units”, 234/17/PU “Błoki 200+”.

**Data Availability Statement:** The data presented in this study are available upon request from the corresponding author. The data are not publicly available due to RAFAKO’s trade secrets.

**Conflicts of Interest:** Authors Piotr Brudziana and Radosław Klon were employed by the company RAFAKO Innovation. The remaining authors declare that the research was conducted in the absence of any commercial or financial relationships that could be construed as a potential conflict of interest.

#### References

1. Kuprianov, V.I.; Kaewklum, R.; Chakritthakul, S. Effects of operating conditions and fuel properties on emission performance and combustion efficiency of a swirling fluidized-bed combustor fired with a biomass fuel. *Energy* **2011**, *36*, 2038–2048. [\[CrossRef\]](#)
2. Qian, X.; Lee, S.; Chandrasekaran, R.; Yang, Y.; Caballes, M.; Alamu, O.; Chen, G. Electricity Evaluation and Emission Characteristics of Poultry Litter Co-Combustion Process. *Appl. Sci.* **2019**, *9*, 4116. [\[CrossRef\]](#)
3. Tillman, D.A. Conventional Power Plant Technology Advances at the End of the 20th Century (1970–2000). In *Coal-Fired Electricity and Emissions Control*; Tillman, D.A., Ed.; Butterworth-Heinemann: Oxford, UK, 2018; pp. 133–167. ISBN 9780128092453. [\[CrossRef\]](#)
4. Pronobis, M. *Environmentally Oriented Modernization of Power Boilers*; Elsevier: Amsterdam, The Netherlands, 2020; ISBN 978-0-12-819921-3. [\[CrossRef\]](#)
5. Roiha, I.; Kaikko, J.; Jaanu, K.; Vakkilainen, E. Analysis of high flue gas recirculation for small energy conversion systems. *Appl. Therm. Eng.* **2014**, *63*, 218–226. [\[CrossRef\]](#)
6. Ling, Z.; Zeng, X.; Ren, T.; Xu, H. Establishing a low-NO<sub>x</sub> and high-burnout performance in a large-scale, deep-air-staging laboratory furnace fired by a heavy-oil swirl burner. *Appl. Therm. Eng.* **2015**, *79*, 117–123. [\[CrossRef\]](#)

7. Niu, Y.; Liu, X.; Wang, S.; Hui, S.; Shaddix, C.R. A numerical investigation of the effect of flue gas recirculation on the evolution of ultra-fine ash particles during pulverized coal char combustion. *Combust. Flame* **2017**, *184*, 1–10. [[CrossRef](#)]
8. Deng, L.; Dong, L.; Bai, Y.; Wu, Y.; Liu, H.; Belošević, S.; Tomanović, I.; Che, D. Effects of flue gas recirculation on combustion and heat flux distribution in 660 MW double-reheat tower-type boiler. *Fuel* **2022**, *321*, 123988. [[CrossRef](#)]
9. Pan, D.; Zhu, T.; Ji, C.; Ke, E. Effects of flue gas recirculation on self-excited combustion instability and NO<sub>x</sub> emission of a premixed flame. *Therm. Sci. Eng. Prog.* **2022**, *30*, 101252. [[CrossRef](#)]
10. Xie, Y.; Liu, X.; Zhang, C.; Wang, H. Numerical investigations on the aerodynamics and flue gas recirculation of cyclone-fired coal boiler. *Fuel* **2022**, *316*, 123355. [[CrossRef](#)]
11. Kim, H.W.; Seo, S.B.; Kang, S.Y.; Go, E.S.; Oh, S.S.; Lee, Y.W.; Yang, W.; Lee, S.H. Effect of flue gas recirculation on efficiency of an indirect supercritical CO<sub>2</sub> oxy-fuel circulating fluidized bed power plant. *Energy* **2021**, *226*, 120487. [[CrossRef](#)]
12. Yan, J.; Zheng, X.; Lu, X.; Liu, Z.; Fan, X. Enhanced combustion behavior and NO<sub>x</sub> reduction performance in a CFB combustor by combining flue gas recirculation with air-staging: Effect of injection position. *J. Energy Inst.* **2021**, *96*, 294–309. [[CrossRef](#)]
13. Liu, J.; Luo, X.; Yao, S.; Li, Q.; Wang, W. Influence of flue gas recirculation on the performance of incinerator-waste heat boiler and NO<sub>x</sub> emission in a 500 t/d waste-to-energy plant. *Waste Manag.* **2020**, *105*, 450–456. [[CrossRef](#)] [[PubMed](#)]
14. Zhang, G.; Xu, W.; Wang, W.; Yang, Y. Analysis and optimization of a coal-fired power plant under a proposed flue gas recirculation mode. *Energy Convers. Manag.* **2015**, *102*, 161–168. [[CrossRef](#)]
15. Huang, X.; Yang, Z.; Ning, K.; Ruan, C.; Chen, C.; Xiao, Y.; Chen, P.; Gu, M.; Zheng, M. Numerical investigation of combustion characteristics under oxygen-enriched combustion combined with flue gas recirculation in a cement rotary kiln. *Appl. Therm. Eng.* **2023**, *233*, 121106. [[CrossRef](#)]
16. Cheng, S.; Kuang, M.; Liu, S.; Qi, S. Lowering further NO<sub>x</sub> emissions and improving the hopper's overheating environment in a low-NO<sub>x</sub> down-fired furnace by a staged arch-firing framework with a primary-burner flue gas recirculation. *Case Stud. Therm. Eng.* **2023**, *51*, 103546. [[CrossRef](#)]
17. Zhou, H.; Yang, Y.; Dong, K.; Liu, H.; Shen, Y.; Cen, K. Influence of the gas particle flow characteristics of a low-NO<sub>x</sub> swirl burner on the formation of high temperature corrosion. *Fuel* **2014**, *134*, 595–602. [[CrossRef](#)]
18. Yang, W.; Rongzhen, Y.; Wang, Z.; Hongtao, Z.; Zhou, Z.; Zhou, J.; Guan, J.; Qiu, L. Effects of Near-Wall Air Application in a Pulverized-Coal 300 MWe Utility Boiler on Combustion and Corrosive Gases. *Energy Fuels* **2017**, *31*, 10075–10081. [[CrossRef](#)]
19. Shim, H.-S.; Valentine, J.R.; Davis, K.; Seo, S.-L.; Kim, T.-H. Development of fireside waterwall corrosion correlations using pilot-scale test furnace. *Fuel* **2008**, *87*, 3353–3361. [[CrossRef](#)]
20. Ma, H.; Zhou, L.; Ma, S.; Du, H. Design of porous wall air coupling with air staged furnace for preventing high temperature corrosion and reducing NO<sub>x</sub> emissions. *Appl. Therm. Eng.* **2017**, *124*, 865–870. [[CrossRef](#)]
21. Available online: <http://www.rafako.com.pl/en/?> (accessed on 2 May 2024).
22. European Commission. *Best Available Techniques Reference Document for the Large Combustion Plants*; Final Draft; European Commission: Brussels, Belgium, 2016.
23. Ansys Fluent. *Computational Fluid Dynamics*; Ansys Inc.: Canonsburg, PA, USA, 2024; Available online: [www.ansys.com](http://www.ansys.com) (accessed on 2 May 2024).
24. Hernik, B. Numerical Research of the Modification of the Combustion System in the OP 650 Boiler. *Energies* **2020**, *13*, 725. [[CrossRef](#)]
25. Pletcher, R.H.; Tannehill, J.C.; Anderson, D.A. *Computational Fluid Mechanics and Heat Transfer*; CRC Press: New York, NY, USA, 2013.
26. Çengel, Y.A.; Cimbala, Y.M. *Fluid Mechanics Fundamentals and Applications*; McGraw-Hill: New York, NY, USA, 2010.
27. Perry, R.H.; Green, D.W. *Chemical Engineers' Handbook*; McGraw-Hill: New York, NY, USA, 1993.
28. Morsi, S.A.; Alexander, A.J. An Investigation of Particle Trajectories in Two-Phase Flow Systems. *J. Fluid Mech.* **1972**, *55*, 193–208. [[CrossRef](#)]
29. Badzioch, S.; Hawksley, P.G.W. Kinetics of Thermal Decomposition of Pulverized Coal Particles. *Ind. Eng. Chem. Process Design Dev.* **1970**, *9*, 521–530. [[CrossRef](#)]
30. Baum, M.M.; Street, P.J. Predicting the Combustion Behavior of Coal Particles. *Combust. Sci. Tech.* **1971**, *3*, 231–243. [[CrossRef](#)]
31. Field, M.A. Rate of Combustion Of Size-Graded Fractions of Char from a Low Rank Coal between 1200 K-2000 K. *Combust. Flame* **1969**, *13*, 237–252. [[CrossRef](#)]
32. Zel'dovich, Y.B. The Oxidation of Nitrogen in Combustion Explosions. *Acta Physicochim. U.S.S.R.* **1946**, *21*, 577–628.
33. Lavoie, G.A.; Heywood, J.B.; Keck, J.C. Experimental and Theoretical Study of Nitric Oxide Formation in Internal Combustion Engines. *Combust. Sci. Tech.* **1970**, *1*, 313–326. [[CrossRef](#)]
34. Fenimore, C.P.; Jones, G.W. The water catalysed oxidation of carbon monoxide by oxygen at high temperatures. *J. Phys. Chem.* **1957**, *61*, 651–654. [[CrossRef](#)]
35. Fenimore, C.P. Formation of Nitric Oxide in Premixed Hydrocarbon Flames. *Symp. (Int.) Combust.* **1971**, *13*, 373–380. [[CrossRef](#)]
36. Warnatz, J. *NO<sub>x</sub> Formation in High Temperature Processes*; University of Stuttgart: Stuttgart, Germany, 2001.
37. Westbrook, C.; Dryer, F. Chemical Kinetic Modelling of Hydrocarbon Combustion. *Prog. Energy Comb. Sci.* **1984**, *10*, 1–57. [[CrossRef](#)]
38. Lockwood, F.C.; Romo-Millanes, C.A. Mathematical Modelling of Fuel—NO Emissions from PF Burners. *J. Int. Energy* **1992**, *65*, 144–152.



39. Winter, F.; Wartha, C.; Loffler, G.; Hofbauer, H. The NO and N<sub>2</sub>O Formation Mechanism During Devolatilization and Char Combustion Under Fluidized Bed Conditions. *Symp. (Int.) Combust.* **1996**, *26*, 3325–3334. [[CrossRef](#)]
40. Brouwer, J.; Heap, M.P.; Pershing, D.W.; Smith, P.J. A Model for Prediction of Selective Non-Catalytic Reduction of Nitrogen Oxides by Ammonia, Urea, and Cyanuric Acid with Mixing Limitations in the Presence of CO. *Symp. (Int.) Combust.* **1996**, *26*, 2117–2124. [[CrossRef](#)]
41. Rota, R.; Antos, D.; Zanoelo, E.F.; Morbidelli, M. Experimental and Modeling Analysis of the NO<sub>x</sub>OUT Process. *Chem. Eng. Sci.* **2002**, *57*, 27–38. [[CrossRef](#)]
42. Orłowski, P.; Dobrzański, W.; Szwarc, E. *Steam Boilers*; WNT: Warszawa, Poland, 1979. (In Polish)
43. Basu, P.; Kefa, C.; Jestin, J. *Boilers and burners. Design and Theory*; Springer: Berlin/Heidelberg, Germany, 2000; ISBN 101771292601.
44. Kuznetsov, N.V.; Mitor, V.V.; Dubovsky, I.E.; Karasina, E.S. *Standards for Thermal Calculations of Power Boilers (Teplovoi Raschet Kotelnih Agregatov)*; Energia: Moskva, Russia, 1973.
45. Pronobis, M. Wymiana ciepła w zanieczyszczonych powierzchniach konwekcyjnych kotłów. *Gliw. Sci. J. Silesian Univ. Technol. Energy*, 1992; ISSN 0372-9796.
46. *PN-EN 12952-15; Water-Tube Boilers and Auxiliary Installations. Acceptance Tests*. PKN: Warszawa, Poland, 2006.
47. Cantrell, C.; Idem, S. On-Line Performance Model of the Convection Passes of a Pulverized Coal Boiler. *Heat Transf. Eng.* **2010**, *31*, 1173–1183. [[CrossRef](#)]
48. Tu, Y.; Zhou, A.; Xu, M.; Yang, W.; Siah, K.B.; Subbaiah, P. NO<sub>x</sub> reduction in a 40 t/h biomass fired grate boiler using internal flue gas recirculation technology. *Appl. Energy* **2018**, *220*, 962–973. [[CrossRef](#)]
49. Baltasar, J.; Carvalho, M.G.; Coelho, P.; Costa, M. Flue gas recirculation in a gas-fired laboratory furnace: Measurements and modelling. *Fuel* **1997**, *76*, 919–929. [[CrossRef](#)]
50. Shalaj, V.V.; Mikhajlov, A.G.; Novikovav, E.E.; Terebilov, S.V.; Novikova, T.V. Gas Recirculation Impact on the Nitrogen Oxides Formation in the Boiler Furnace. *Procedia Eng.* **2016**, *152*, 434–438. [[CrossRef](#)]
51. Bosoaga, A.; Panoiu, N.; Mihaescu, L.; Backreedy, R.I.; Ma, L.; Pourkashanian, M.; Williams, A. The combustion of pulverised low grade lignite. *Fuel* **2006**, *85*, 1591–1598. [[CrossRef](#)]
52. Nielsen, H.P.; Frandsen, F.J.; Dam-Johansen, K.; Baxter, L.L. The implications of chlorine-associated corrosion on the operation of biomass-fired boilers. *Prog. Energy Combust. Sci.* **2000**, *26*, 283–298. [[CrossRef](#)]
53. Hernik, B. Research to Reduce the Corrosion and Erosion Hazard of Boilers. Ph.D. Thesis, Silesian University of Technology, Gliwice, Poland, 2009. (In Polish).
54. Pronobis, M.; Hernik, B.; Wejkowski, R. Kinetics of low NO<sub>x</sub> corrosion of waterwalls in utility boilers. *Rynek Energi* **2010**, *6*, 121–128.

**Disclaimer/Publisher’s Note:** The statements, opinions and data contained in all publications are solely those of the individual author(s) and contributor(s) and not of MDPI and/or the editor(s). MDPI and/or the editor(s) disclaim responsibility for any injury to people or property resulting from any ideas, methods, instructions or products referred to in the content.